JOINT INSTITUTE FOR NUCLEAR RESEARCH

Annotation on Project

"Studies of Baryonic Matter at the Nuclotron (BM@N)"

02-0-1065-2007/2023

LEADER M.N.Kapishin

Submitted

LHEP Science and Technology Council

LIST OF PARTICPANTS FROM JINR AND MEMBER-STATES

Joint Institute for Nuclear Research – JINR (Dubna), FTE = 82
K. Abraamyan, S.V.Afanasiev, G.N.Agakishiev, I.N. Aleksandrov, E.I. Aleksandrov, K.A. Alishina, T. Atovullaev, V.A.Babkin, V.P. Balandin, N.A.Balashov, D.A.Baranov, P.N.Batyuk, M. Baznat, S.N.Bazylev, M.G.Buryakov, D.N.Bogoslovsky, V.E. Burtsev, S.G. Buzin, A.I. Chebotov, B.Dabrowska, D.V. Dementev, A.V.Dmitriev, D.K.Dryablov, P.O. Dulov, D.S.Egorov, V.V. Elsha, A.A.Fediunin, I.A.Filippov, I.A. Filozova, I.R. Gabdrakhmanov, O.P.Gavrischuk, K.V.Gertsenberger, V.M.Golovatyuk, M.N.Kapishin, V.Yu.Karjavin, R.R.Kattabekov, V.D.Kekelidze, S.V.Khabarov, Yu.T.Kiryushin, V.I.Kolesnikov, A. Kolozhvari, Y.A.Kopylov, A.D. Kovalenko, Y.S. Kovalev, E.M.Kulish, S.N.Kuklin, A.Kuznetsov, E.A.Ladygin, N.A. Lashmanov, V.V.Lenivenko, E.I.Litvinenko, S.P.Lobastov, A.M. Makan'kin, A.I.Maksymchyuk, A.I.Malakhov, G.J.Musulmanbekov, S.P.Merts, A.N.Morozov, Yu.A.Murin, R.V.Nagdasev, D.N.Nikitin, D.A.Oleynik, V.V.Palchik, M.A.Patsyuk, Yu.P.Petukhov, A. Petrosyan, S.M.Piyadin, V.A.Plotnikov, D.Podgainy, Yu.K.Potrebenikov, O.V.Rogachevsky, V.Yu.Rogov, P.A.Rukoyatkin, I.A.Rufanov, M.M.Rumyantsev, D.G. Sakulin, S.A.Sedykh, S.V.Sergeev, A.D.Sheremetev, A.I.Sheremeteva, A.V. Shchipunov, M.O.Shitenkov, A.V.Shutov, V.B.Shutov, I.V.Slepnev, V.M.Slepnev, I.P.Slepov, A.S.Sorin, V.N.Spaskov, E.A.Streletskaya, O.I.Streltsova, N.V.Sukhov, D.A.Suvarieva, N.A. Tarasov, O.G.Tarasov, A.V.Terletsky, V.V.Tikhomirov, A.A. Timoshenko, O.V.Teryaev, N.D.Topilin, B.L. Topko, Yu.Topko, I.A.Tyapkin, V.A.Vasendina, A.V.Vishnevskiy, A.Voronin, N.Voytishin, V.I.Yurevich, N.I.Zamiatin, M. Zavertyaev, Al.I.Zinchenko, V.N.Zhezher, E.V.Zubarev, M.I.Zuev

Institute for Nuclear Research RAS (Moscow)
A.I.Baranov, D. Finogeev, D.Gerasimov, M.B.Golubeva, F.F.Guber, A.P.Ivashkin, A.V. Izvestnyy, N.M.Karpushkin, A.Makarov, A.I. Makhnev, S.V.Morozov, O.A.Petukhov, A.I. Reshetin, E.Zherebtsova

Institute for Theoretical Experimental Physics – ITEP (Moscow)
P. Alekseev, D.Yu.Kirin, I.Larin, V.Semyachkin, A.V.Stavinsky, V.Tarasov, N.Zhigareva

Skobeltsyn Institute of Nuclear Physics Moscow State University (Moscow)
A. Baranov, N. Baranova, G. Bogdanova, E. Boos, D. Karmanov, P. Kharlamov, M. Korolev, I. Kovalev, I. Kudryashov, A. Kurganov, V. Kukulin, D. Lanskoy, V. Leontiev, M.M.Merkin, M. Platonova, A.Solomin, T. Tretyakova, V. Volkov, A. Voronin

Moscow Institute of Physics and Technology – MIPT (Moscow)
T.Aushev, P. Klimai

Moscow Engeenering Physics Institute – MEPhI (Moscow)
E.Atkin, N.Barbashina, A.Bolozdynya, K.Filippov, A.Galavanov, V.Samsonov, I.Selyuzhenkov, P.Senger, V.Shumikhin, V.Sosnovtsev, M.Strikhanov, A.Taranenko

Kurchatov Inst. NRC, Moscow
D.Blau, D. Peresunko

SPbU, St Petersburg
A.Dryuk, S.Nemnyugin, V.Roudnev, M.Stepanova

Bulgaria
Plovdiv University ”Paisii Hilendarski” (Plovdiv)
V.D.Tcholakov, L.Kovachev, M.Shopova, V.Kabadzhov

China
Key Laboratory of Nuclear Physics and Ion-Beam Application (MOE), Institute of Modern Physics, Fudan University, Shanghai
Y.Ma, J.Chen, S.Zhang

Czech republic
Nuclear Physics Institute, CAS, Řež
P.Chudoba, A.Kugler, V.Kushpil, S.Kushpil, V.Mikhaylov

Germany
GSI, Darmstadt
U.Frankenfeld, J.Heuser, R.Kapell, A.Lymanets, C.Schmidt, H.R.Schmidt, P.Senger, M.Teklishyn

Tubingen U., Tubingen
I.Panasenko, H.R.Schmidt, E.Volkova

Poland
Warsaw University of Technology, Faculty of Physics (Warsaw)
D. Dąbrowski, G. Kasprowicz, A. Kisiel, M. Lawryńczk, M. Linczuk, M. J. Peryt, S. Plamowski, J. Pluta, K. Poźniak, P. Rokita, R. Romaniuk, K. Roslon, T. Starecki, T. Traczyk, P. Wieczorek, D. Wielanek, W. Zabolotny

University of Wroclaw, Wroclaw
D. Alvear-Terrero, D. Blaschke, A. Ciszewski, R. Lewandkow, A. Sedrakian, O. Warmusz

Project leader:	M.Kapishin (JINR)
Project depity:	A.Maksymchuk (JINR)

Content:

1.Introduction

The theoretical and experimental investigation of the properties strongly interacting matter at high temperatures and densities is one of the most exciting research programs of modern high-energy nuclear physics. The recent astronomical observations of supermassive neutron stars and neutron star mergers challenge our knowledge on high-density QCD matter, like its equation-of- state (EOS) and its microscopic degrees-of-freedom at high baryon densities. Future measurements of mass and radius of neutron stars and the precise spectroscopy of gravitational waves will improve our understanding of the high-density EOS. Complementary information will be obtained by laboratory experiments with energetic heavy-ion collisions, which provide the opportunity to investigate both the EOS at high density, and to explore the degrees-of-freedom of this matter, including the search for new phases of high-density matter, which possibly feature characteristic structures like critical points. The investigation of the QCD phase diagram is a worldwide endeavor undertaken at heavy-ion accelerators like LHC and SPS at CERN, RHIC at BNL, and SIS18 at GSI. Future projects, like the "Facility for Antiproton and Ion Research" (FAIR) [1.1] in Darmstadt, Germany, and the "Nuclotron-based Ion Collider fAcility" (NICA) [1.2], will open unique possibilities to produce and explore QCD matter at densities, which are predicted to exist in the core of neutron stars. In particular, the fixed-target Compressed Baryonic Matter (CBM) experiment at FAIR [1.3], and the Multi-Purpose Detector (MPD) at the NICA collider [1.4] will focus on the investigation of diagnostic probes which are sensitive to the EOS and the degrees-of-freedom of high-density QCD matter. The existing Baryonic Matter @Nuclotron (BM@N) [1.5] experiment will be upgraded, in order to investigate heavy-ion collisions at beam energies up to about 4A GeV, where the fireball is predicted to be compressed to about 4 times saturation density.

2. Physical motivation: BM@N heavy ion physics program

The future Nuclotron beams are well suited to produce dense nuclear matter in the collision of heavy nuclei. In central Au + Au collision at top Nuclotron beam beam energies, densities of 4 -5 times saturation densities will be reached in the center of the reaction volume [2.1], corresponding to the densities prevailing in the core of neutron stars. Like matter in compact stellar objects, the matter in this fireball will be compressed according to the equation-of-state (EOS), and experiments at the Nuclotron, but also at NICA and at FAIR may shed light on the properties of neutron stars. These laboratory experiments complement astronomical observations of mass and radii of neutron stars, in order to determine the high-density EOS. Laboratory measurements, however, might be also sensitive to the degrees-of-freedom of dense nuclear, which are expected to change with increasing density, when the nucleons overlap and start to melt into their elementary constituents. Moreover, heavy-ion experiments may also provide information on the role of hyperons in neutron stars. The main aspects of the physics program of the BM@N experiment and the relevant observables will be discussed in the following.

2.1 The Nuclear-Matter Equation-of-State

The nuclear matter equation-of-state (EOS) relates thermodynamic properties like pressure, volume, temperature etc., and can be written as the energy per nucleon as a function of density:

$$E_A(\rho,\delta) = E_A(\rho,0) + E_{sym}(\rho)\cdot\delta^2 + O(\delta^4)$$

where the first term represents the EOS for symmetric matter, and the second term is the symmetry energy with $\delta = (\rho_n - \rho_p)/\rho$ the isospin asymmetry parameter. The EOS of symmetric matter is commonly parameterized by the binding energy per nucleon at saturation density ρ_0 and the incompressibility K_{nm}, which corresponds to the curvature around ρ_0. Several versions of the EOS for symmetric matter are represented by the lower curves in figure 2.1 [2.2]. The EOS for neutron matter is represented by the upper curves in figure 2.1, and the difference between the upper and lower curves for each EOS is the symmetry energy E_{sym}.

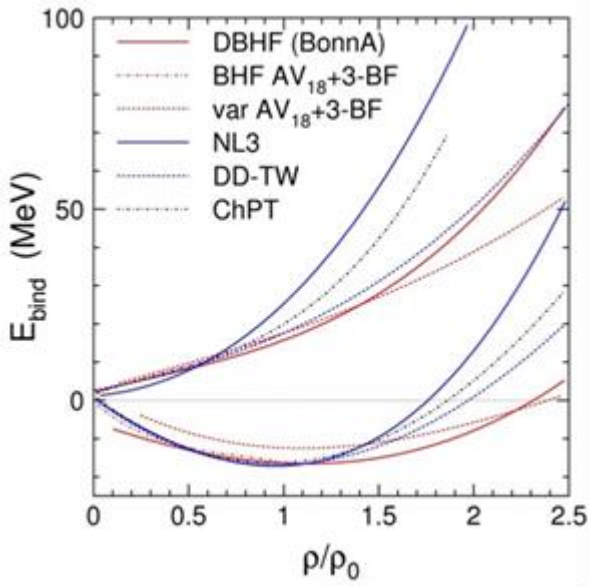

Fig. 2.1: Different versions of the equation of state for isospin-symmetric nuclear matter (lower curves) and for neutron matter (upper curves). For more information see [2.2].

Experiments at GSI have been performed by the FOPI collaboration, which measured the elliptic flow of protons, deuterons, tritons, and ^{3}He in Au + Au collisions at beam kinetic energies between 0.4 and 1.5 A GeV [2.3]. The elliptic flow of particles is driven by the pressure gradient in the reaction volume, and, therefore, is sensitive to the EOS. The FOPI data have been interpreted by calculations using the isospin-dependent quantum molecular dynamics (IQMD) transport code [2.3]. It was found, that the data can be explained assuming a nuclear incompressibility of K_{nm} = 190 ± 30 MeV, which corresponds to a soft EOS for symmetric nuclear matter up to nuclear densities of about 2-3 ρ_0.

In order to contribute to our understanding of neutron stars, densities of 4-5 ρ_0 have to be produced and investigated. Even higher densities have been reached in experiments at the AGS in Brookhaven, which measured both the directed and the elliptic flow of protons in Au + Au collisions at energies between 2 and 11 A GeV [2.4]. It turned out, that the data on directed flow agree with the assumption of a soft EOS, whereas the elliptic flow data point towards a hard EOS [2.5]. In conclusion, the interpretation of these data did not much constrain the range of possible EOS at high densities, and one important goal of the BM@N research program is to improve these flow measurements.

An alternative approach to study the EOS of symmetric matter is to investigate subthreshold strangeness production in heavy-ion collisions. This method has been pioneered by the KaoS collaboration at GSI, which measured the excitation function of K^+ meson production in Au + Au and C + C collisions beam energies from 0.8 and 1.5 A GeV [2.6]. The minimum energy to create a K^+ meson in nucleon-nucleon collisions, for example via the process $p+p \rightarrow K^+\Lambda p$, is 1.58 GeV. Therefore, at sub-threshold energies, strangeness has to be produced via multiple collisions involving pions and Delta resonances. These sequential collisions occur more frequently, if the baryon density is high, which means, that the EOS is soft. The EOS effects show up in the heavy Au+Au system, but are be less pronounced in the small C+C system. The kaon yield ratio from Au+Au over C+C collisions clearly exhibits an enhancement towards lower beam energies, which is caused by a soft EOS with a nuclear incompressibility of $K_{nm} \approx 200$ MeV according to RQMD and IQMD transport calculations [2.7,2.8]. This result agrees with the elliptic flow measurements done by FOPI in the same energy range, covering baryon densities up to about twice saturation density.

Another very promising observable sensitive to the high-density EOS of symmetric matter is the excitation function of multi-strange (anti-)hyperons. According to transport models, Ξ and Ω hyperons are produced in sequential collisions involving kaons and Λ hyperons, and, therefore, are sensitive to the density in the fireball [2.9,2.10]. This sensitivity is expected to increase at beam

energies close to or even below the production threshold. For example, the production of a Ξ^- hyperon in a proton-proton collision $pp \rightarrow \Xi^- K^+K^+p$ requires a minimum proton energy of E_{thr} = 3.7 GeV. Nevertheless, Ξ^- hyperons can be produced in heavy-collisions via strangeness exchange reaction at energies above the lambda threshold of 1.6 GeV via lambda-lambda collisions $\Lambda^0\Lambda^0 \rightarrow \Xi^- p$. Even Omega hyperons can be produced, when the Xi collides with another lambda $\Lambda^0 \Xi^- \rightarrow \Omega^- n$ or with a kaon $K^- \Xi^- \rightarrow \Omega^- \pi^-$. Therefore, the measurement of multi-strange hyperons will be a central goal of the BM@N research program at the Nuclotron.

2.2 Mixed Phases of QCD Matter

In central Au+Au collisions at top Nuclotron beam energies, baryon densities of more than 4-5 ρ_0 might be reached. At these densities, the nucleons may already partly overlap, and start to melt into their elementary constituents. The question is, which observable might be sensitive to this onset of deconfinement? At very high bombarding energies like at LHC, there is experimental and theoretical evidence for the creation of a deconfined phase, the socalled Quark-Gluon-Plasma (QGP). One of the arguments is, that the yield of all created hadrons can be perfectly explained by the statistical hadronization models, assuming chemical equilibrium in a fireball with a temperature of about 156 MeV and vanishing baryon-chemical potential [2.11]. In particular the observation, that also multi-strange (anti-) hyperons are equilibrated, although their scattering cross section with nucleons is small, has been interpreted as indication for a phase transition from partonic to hadronic matter, which drives the hyperons into equilibration [2.12]. The same observation was made for Pb+Pb collisions at a beam kinetic energy of 30A GeV at the SPS for a fireball temperature 138 MeV of and a baryon-chemical potential of 380 MeV [2.13]. At much lower beam energies, i.e. in Ar + KCl collisions at an energy of 1.76A GeV, most of the hadron yields are also compatible with the statistical model for a temperature of 76 MeV and a baryon-chemical potential of 800 MeV. The yield of Ξ^- hyperons, however, exceeds the model prediction by about a factor 24 ± 9 [2.14]. This high yield is generated by multiple collisions including strangeness exchange reactions in a hadronic environment, as discussed above. Obviously, the Ξ^- hyperons did not equilibrate, because the beam energy is too low to for a phase transition. The energies at the Nuclotron might be sufficiently high to see the onset of deconfinement. Therefore, the BM@N research program includes the measurement of the excitation function of multi-strange hyperons in Au + Au collisions in order to explore the onset of equilibration of multi-strange hyperons at high net-baryon densities.

2.3. Hyperons in Dense Nuclear Matter

The role of hyperons in neutron stars is still a puzzle. If the hyperon chemical potential in dense nuclear matter falls below the chemical potential of neutrons and protons, these particles will decay in to hyperons. This process is expected to occur in the core of neutron stars at densities above 4 – 5 ρ_0, leading to a softening of the nuclear equation-of-state, and, hence, preventing the existence of high mass neutron stars. On the other hand, neutron stars with about twice the mass of our sun have been observed [2.15]. The hyperon chemical potential depends not only on the repulsive two-body hyperon-nucleon ΛN force, but also on the three-body repulsive ΛNN interaction, which becomes increasingly important at high densities [2.16]. Therefore, laboratory experiments devoted to the investigation of hyperon-nucleon interactions will shed light on the role of hyperons in neutron stars. One possibility to study these interactions is to discover new hypernuclei and to measure their lifetimes. According to statistical model and transport calculations, light hypernuclei and even double-lambda hypernuclei are abundantly produced in heavy-ion collisions at Nuclotron and NICA energies [2.17,2.18]. This opens the opportunity for the upgraded BM@N experiment, to measure light hypernuclei in Au+Au collision at the top Nuclotron beam energy, and to contribute to the solution of the long-standing hyperon puzzle in neutron stars.

References

[1.1] https://fair-center.de

[1.2] https://nica.jinr.ru

[1.3] T. Ablyazimov et al., [CBM Collaboration] Eur. Phys. J. A 53 (2017) 60

[1.4] V. Golovatyuk et al., Nucl. Phys. A 982 (2019) 963

[1.5] M. Kapishin for the BM@N collaboration, Nucl. Phys. A 982 (2019) 967

[2.1] I.C. Arsene et al., Phys. Rev. C 75, 24902 (2007)

[2.2] C. Fuchs, arXiv:nucl-th/0610038

[2.3] A. Le Fevre et al., Nucl. Phys. A 945 (2016) 112–133.

[2.4] C. Pinkenburg et al., Phys. Rev. Lett. 83 (1999) 1295.

[2.5] P. Danielewicz, R. Lacey, W.G. Lynch, Science 298 (2002) 1592.

[2.6] C. Sturm et al. [KaoS Collaboration] Phys. Rev. Lett. 86 (2001) 39.

[2.7] Ch. Fuchs et al., Phys. Rev. Lett. 86 (2001) 1974

[2.8] C. Hartnack and J. Aichelin, J. Phys. G 28 (2002) 1649.

[2.9] F. Li et al., Phys. Rev. C 85 (2012) 064902

[2.10] G. Graef et al., Phys. Rev. C 90 (2014) 064909

[2.11] A. Andronic et al., J. Phys. G38 (2011) 124081

[2.12] P. Braun-Munzinger, J. Stachel and C. Wetterich, Phys.Lett. B 596 (2004) 61

[2.13] A. Andronic, P. Braun-Munzinger and J. Stachel, Acta Phys. Polon. B 40 (2009) 1005

[2.14] G. Agakishiev et al. [HADES collaboration] Eur. Phys. J. A 47 (2011) 21

[2.15] H. T. Cromartie et al., Nat. Astron. 2019, doi:10.1038/s41550-019-0880-2.

[2.16] W. Weise, arXiv:1905.03955v1, to appear in JPS Conf. Proc

[2.17] A. Andronic et al., Phys. Lett. B 697 (2011) 203

[2.18] A. S. Botvina et al., Phys. Lett. B 742 (2015) 7

3. Detector for studies of Baryonic Matter at Nuclotron (BM@N)

BM@N (Baryonic Matter at Nuclotron) is the first experiment at the accelerator complex of NICA Nuclotron. The heavy-ion physics program of the NICA accelerator complex and the MPD experiment planned at the NICA collider are described in [3.1-3.4]. The aim of the BM@N experiment is to study interactions of relativistic heavy ion beams with fixed targets [3.5]. The Nuclotron will provide verity of beams from protons to gold ions with the kinetic energy of ions ranging from 1 to 6 GeV per nucleon. The maximum kinetic energy for ions with the ratio of the charge to the atomic weight (Z/A) of 1/2 is 6 GeV per nucleon. The maximum kinetic energy for heavy ions with the ratio of Z/A ~ 1/3 is 4.5 GeV per nucleon. The maximum kinetic energy of protons is 13 GeV. The beam line between the Nuclotron and the BM@N experiment is around 160 meter in length. It comprises 26 elements of magnetic optics: 8 dipole magnets and 18 quadruple lenses. An upgrade program of the beam line is foreseen to minimize the amount of scattering material on the way of heavy ions to the BM@N setup.

The planned intensity of the gold ion beam at BM@N is few 10^6 ions/s. The acceleration of the gold ion beam is planned after the Nuclotron upgrade in 2022. In Fig. 3.2 the interaction rates are presented for different experiments with heavy ion collisions at different energies per nucleon-nucleon collision in the center of mass system. The beam energy of the BM@N experiment is in the intermediate range between experiments at the SIS-18 and NICA/FAIR facilities and partially overlaps the energy range of the HADES experiment. The acquisition rate of non-peripheral

collisions, i.e., central or intermediate interactions is expected to range from 20 to 50 kHz at the second stage of the BM@N experiment in 2022 and later. The interaction rate is limited by the capacity of the data acquisition system and readout electronics.

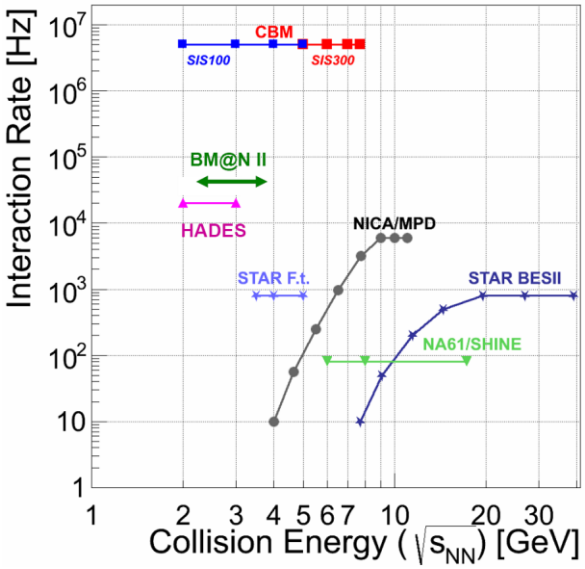

Figure 3.2 Heavy ion experiments: interaction rate and nucleon-nucleon collision energy in c.m.s.

References

[3.1] G. Trubnikov, A. Kovalenko, V. Kekelidze, I. Meshkov, R. Lednicky, A. Sissakian, A. Sorin, PoS (ICHEP 2010) 523.

[3.2] G. Trubnikov, N. Agapov, V.Kekelidze, A. Kovalenko, V. Matveev, I.Meshkov, R. Lednicky, A. Sorin, PoS 36th International Conference of High Energy Physics (ICHEP2012), July 4-11,Melbourne, Australia.

[3.3] V. Kekelidze, A. Kovalenko, R. Lednicky, V. Matveev, I.Meshkov, A. Sorin, G. Trubnikov, 37th International Conference on High Energy Physics, ICHEP 2014, July 2-9, Valencia, Spain, Nuclear physics B Proceedings supplements (2014).

[3.4] V. Kekelidze, Multi-purpose detector (MPD) of the collider experiment, these proceedings.

[3.5] BM@N Conceptual Design Report.

http://nica.jinr.ru/files/BM@N/BMN_CDR.pdf

[3.6] J. Heuser et al., Technical Design Report for the CBM Silicon Tracking System, CBM Collaboration, GSI Report 2013-4,

http://repository.gsi.de/record/54798

3.1 Main characteristics of the experimental setup

The layout of the proposed BM@N configuration for heavy ion program is shown in Fig. 3.1.1. The experiment combines high precision measurement of track parameters with time-of-flight information for particle identification and presumes a measurement of the total energy by the hadron calorimeter to analyze the collision centrality. The charged track momentum and multiplicity will be measured using a set of forward silicon detectors (FwdSi), large aperture silicon tracking system (STS), 7 planes of two-coordinate GEM (Gaseous Electron Multiplier) detectors mounted downstream of the target inside of the analyzing magnet. The GEM detectors are operational at high particle densities and in strong magnetic fields. The vertical gap between the poles of the analyzing magnet for detector installation is about 1 m. The magnetic field can reach a maximum value of 1 T, which makes it possible to optimize the BM@N geometrical acceptance and resolution on momentum for different processes and energies of the beam. The outer tracking

system will consist of cathode strip chambers which will supplement the existing drift chambers to increase the effectiveness of track measurement in Au+Au collisions. The time-of-flight detectors (ToF) based on the multi-gap Resistive Plate Chamber (mRPC) technologies with strip readout provide an opportunity to separate hadrons (π, K, p) and light nuclei with momentum up to few GeV/c. The Zero Degree Calorimeter (ZDC) detector is foreseen for the extraction of the collision impact parameter (centrality) by measuring the energy of the fragments of colliding particles. The scintillator multiplicity Barrel detector positioned around the target and partially overlapping the backward hemisphere is planned to generate a trigger signal for the data acquisition system. A set of beam trigger detectors will also provide a starting signal (T0) for the time-of-flight detectors.

In 2022, after the heavy ion program upgrade, the BM@N experiment will start with middle size ion (Kr,Xe) beams. At this stage the hybrid central tracker will consist of three two-coordinate planes of the FwdSi detectors and 7 planes of the GEM detectors as it is shown in Fig.3.1.2. The results of simulations for this configuration of the central tracker are givent in section 3.2.2. In 2023 it is planned to add two pilot two-coordinate planes of the STS detectors to extend the capacity of the central tracker to run with heavy ion beams. The stages of the BM@N experiment from the starting technical runs to the final high intensity runs with heavy ion beams are given in Table 3.1.

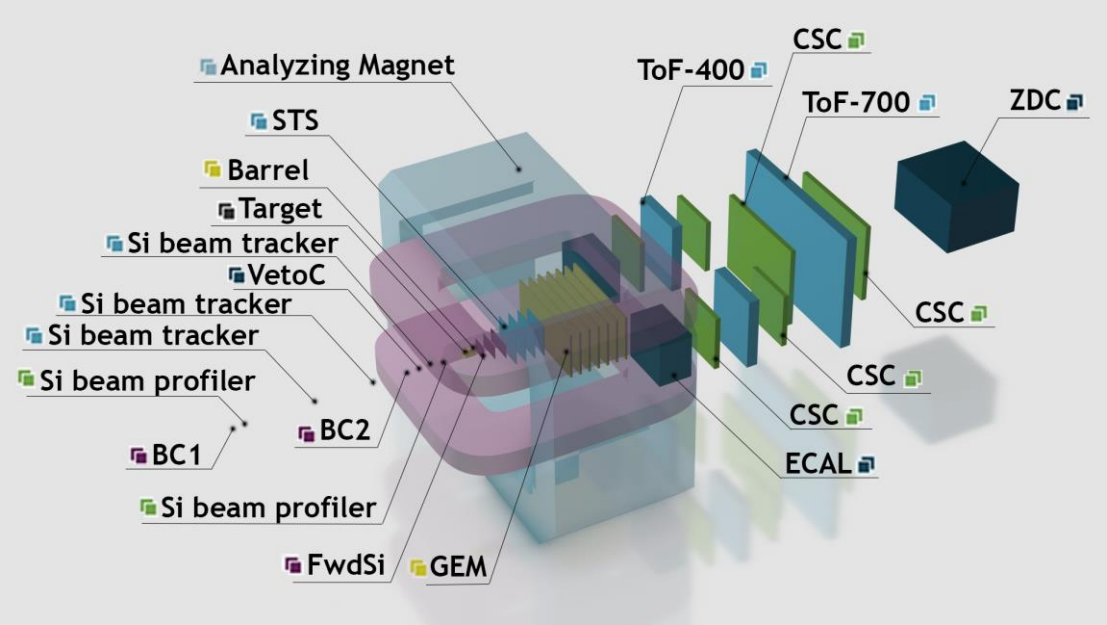

Figure 3.1.1. Schematic view of the BM@N setup for the heavy ion program (without vacuum beam pipe). .

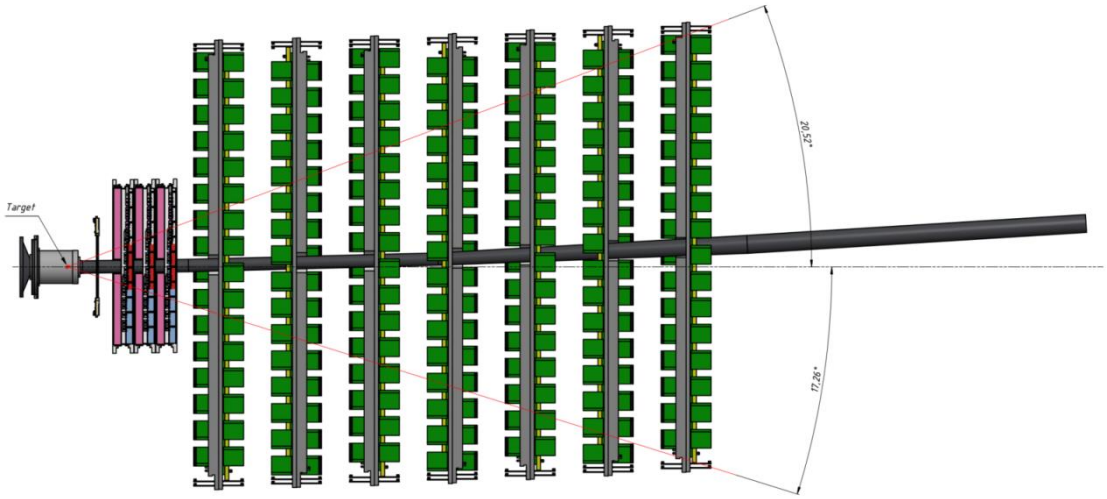

Figure 3.1.2. Schematic view of the initial hybrid tracker based on 3 forward silicon planes and 7 GEM planes. The carbon vacuum beam pipe follows the trajectory of the beam.

At the second stage of the BM@N experiment after 2023, four two-coordinate planes of the STS detectors will be installed in front of the GEM detectors to improve track reconstruction in heavy ion collisions (Fig. 3.1.3). Detectors of this type are currently under development in cooperation with the CBM experiment, therefore the actual implementation of the STS tracker upgrade depends on the timetable of the CBM silicon tracker program. The STS FEE electronics is cabable to register interactions with the event rate of 50 kHz, which is the primary goal of the BM@N experiment (see Fig. 3.2). To record interactions with the 50 kHz rate, the FEE electronics of the GEM detectors should be upgraded to a faster version, which is presently under development.

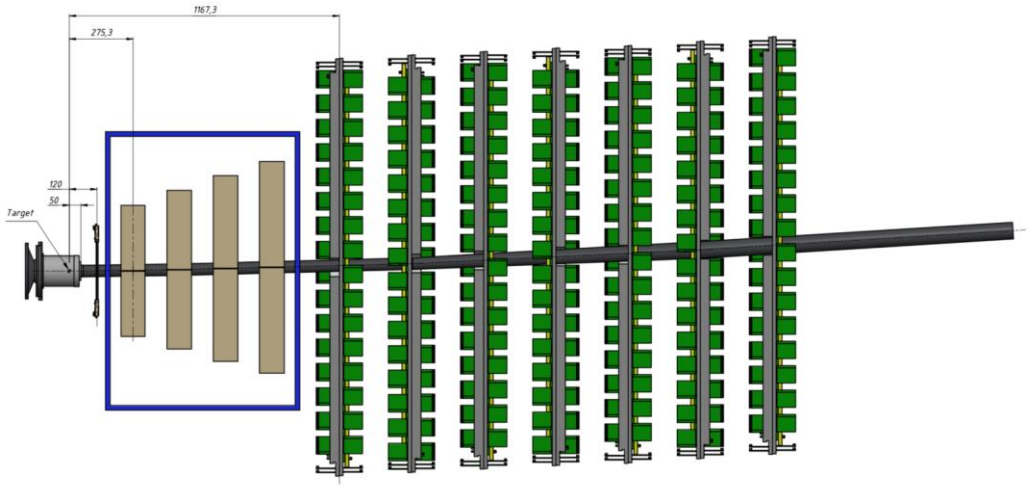

Figure 3.1.3. Schematic view of the final hybrid tracker based on 4 large apperture planes of silicon tracking system and 7 GEM planes.

Table 3.1. Configuration of the BM@N central tracker, beam parameters and event rates in BM@N experimental runs

Year	2016-2017 spring	2018 spring	2022 spring	2023	after 2023
Beam	d, C	Ar,Kr, C(SRC)	Kr,Xe	up to Au	up to Au
Beam intensity, Hz	0.5 M	0.5 M	0.5 M	0.5 M	2 M
Data rate, Hz	5 k	10 k	10 k	20 k	50 k
Central tracker configuration	6 GEM half-planes	6 GEM half-planes + 3 small FwdSi planes	6 GEM full planes + 3 FwdSi full planes	7 GEM planes + 4 FwdSi planes + 2 STS planes	7 GEM planes + + 4 STS planes
Status of the experiment	Technical run	Technical run	Physics run, first stage	Physics run	High rate physics run, second stage

3.2 BM@N performance and feasibility study

3.2.1 BM@N performance in the first experimental runs

Technical runs with the BM@N detector were performed in the deuteron beam in December 2016 and in the carbon beam in March 2017. The kinetic energy was 4 GeV/nucleon for the deuteron beam and was varied from 3.5 to 4.5 GeV/nucleon for the carbon beam. The configuration of the BM@N set-up in these runs is shown in Fig.3.2.1.1. The central tracker set-up comprised a forward silicon strip Si plane, 5 two coordinate GEM detectors with the size of 66 x 41 cm^2 and two GEM detectors with the size of 163 x 45 cm^2. The GEM detectors were combined into 6 GEM stations. All the GEM detectors are two coordinate detectors and have the strip pitch of 800 μm. The inclination angles of the X and X' coordinates of the GEM detectors to the vertical axis are 0 and 15 degree, respectively. The beam crossed the GEM detectors in the middle of the sensitive planes. The experimental data from the central tracker, outer drift chambers, time-of-flight detectors, zero degree calorimeter and trigger detectors were read out using the integrated data acquisition system.

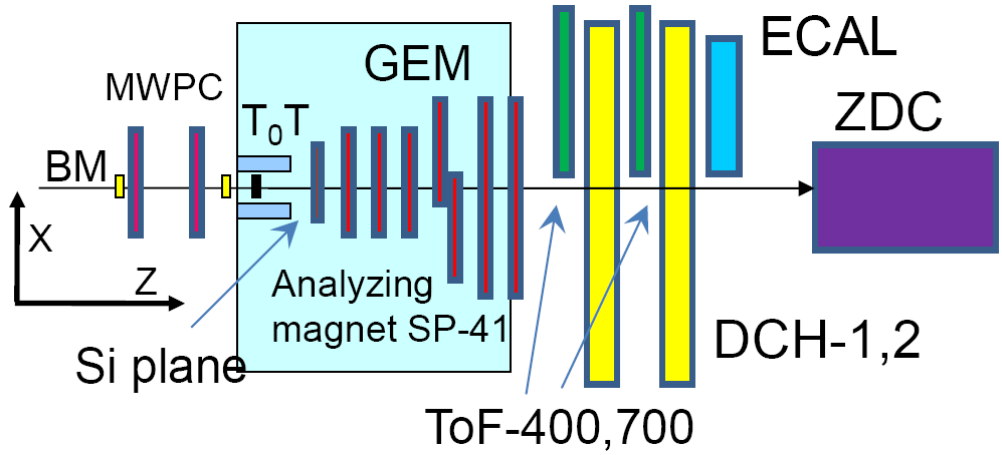

Figure 3.2.1.1 Schematic view of the BM@N setup in the experimental run with the carbon beam.

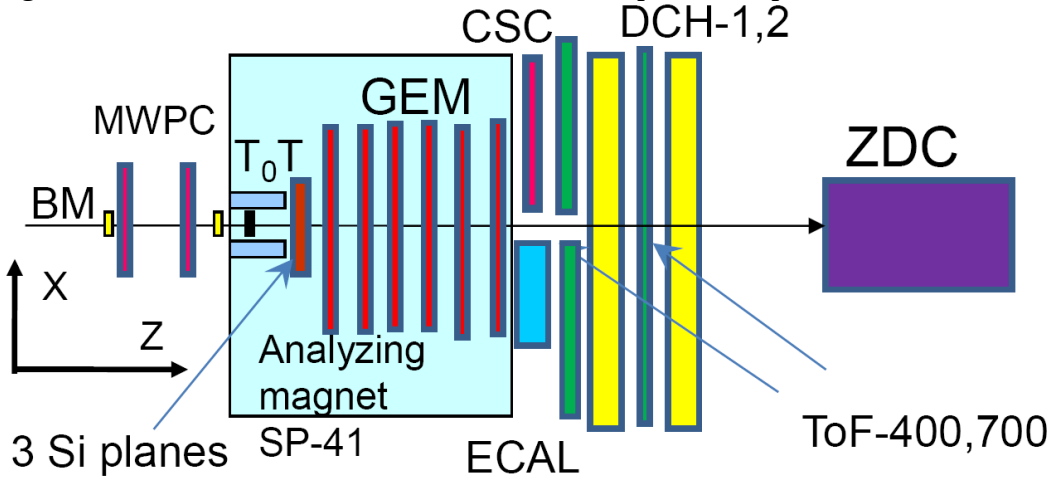

Figure 3.2.1.2 Schematic view of the BM@N setup in the experimental run with the argon and krypton beams.

Figure.3.2.1.3 View of the BM@N setup (left plot) and the GEM tracker (right plot) in the experimental run with the argon and krypton beams in March 2018.

The extended configuration of the BM@N set-up was realized in the next runs with the argon and krypton beams performed in March 2018. The schematic view of the set-up is shown in Fig. 3.2.1.2. The photos of the set-up are given in Fig.3.2.1.3. The set-up comprised six 2-coordinate planes GEM detectors with the size of 163 x 45 cm2, three forward silicon strip Si planes, outer tracker based on two drift chambers DCH and a cathode strip chamber CSC, full time-of-flight system consisting of ToF-400 and ToF-700, extended trigger system T_0T, hadron ZDC and electromagnetic ECAL calorimeters. The GEM tracking detectors covered only the upper half of the acceptance within the analyzing magnet. The collected data were used to check efficiencies of sub-detectors and develop algorithms for the event reconstruction and analysis. In particular, experimental data of minimum bias interactions of the beam with different targets were analyzed with the aim to reconstruct tracks, primary and secondary vertices using the central tracking detectors [3.2.8–3.2.11]. The track reconstruction method was based on the so-called 'cellular automaton' approach [3.2.13]. . Since the GEM tracker configuration in the carbon run was tuned to measure relatively high-momentum beam particles, the geometrical acceptance for relatively soft decay products of strange V0 particles was rather low. The Monte Carlo simulation showed that only ~4% of Λ hyperons and ~0.8% of K0s could be reconstructed.

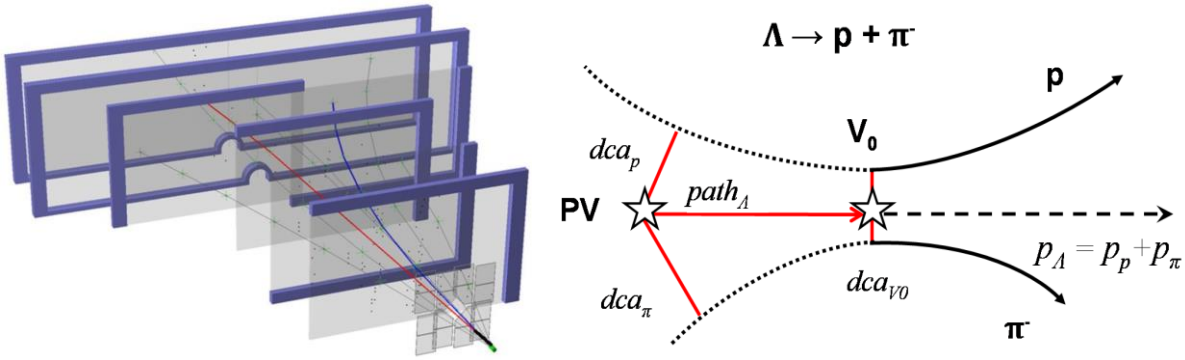

Figure 3.2.1.4 Left plot: Event of Λ hyperon production in a carbon-nucleus interaction reconstructed in the central tracker. Right plot: Topology of Λ→pπ⁻ decay and variables used to select Λ hyperons.

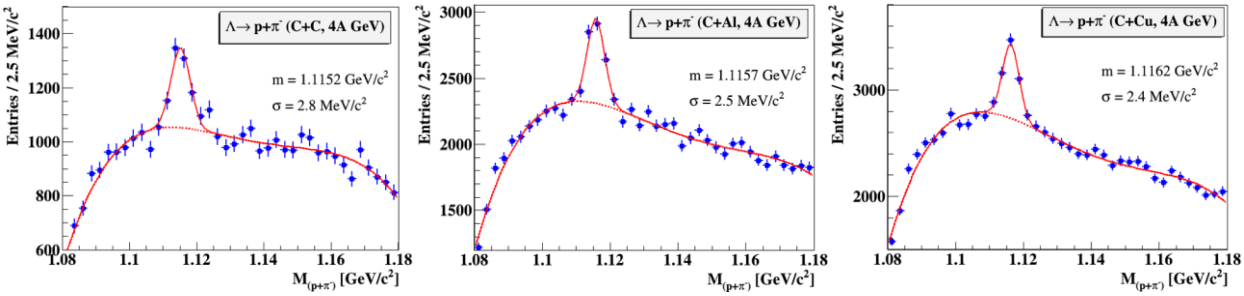

Figure 3.2.1.5 Λ hyperon signals in the invariant mass spectrum of (p, π^-) pairs reconstructed in interactions of the 4 AGeV carbon beam with the C,Al,Cu targets.

Λ hyperons were reconstructed using their decay mode into (p, π^-) pairs as illustrated at Fig.3.2.1.4. Since particle identification at this stage of the analysis was not used, all positive tracks were considered as protons and all negative as π^-. The invariant mass distributions of (p,π^-) pairs are shown in Fig. 3.2.1.5 for reconstructed interactions of the carbon beam with the C, Al, Cu targets. The background under the signal will be reduced by introducing additional silicon tracking detectors to improve the primary and decay vertex resolution. The yields of Λ hyperons in minimum bias interactions of the 4 AGeV carbon beam with the C, Al, Cu targets are measured in the kinematic range on the Λ transverse momentum of $0.1 < p_T < 1.05$ GeV/c and the Λ rapidity in c.m.s. of $0.03 < y^* < 0.93$ [3.2.12] . The y^* and p_T spectra of the Λ hyperon yields corrected for the

detector acceptance and efficiency are presented in Fig.3.2.1.6. The measured yields of Λ hyperons in minimum bias C+C interactions are extrapolated into the full kinematic range using averaged predictions of the DCM-QGSM [3.2.15] and UrQMD models. The Λ yield measured by BM@N is compared in Fig.3.2.1.6 with the results of other experiments [3.2.16–3.2.18] and with the model predictions.

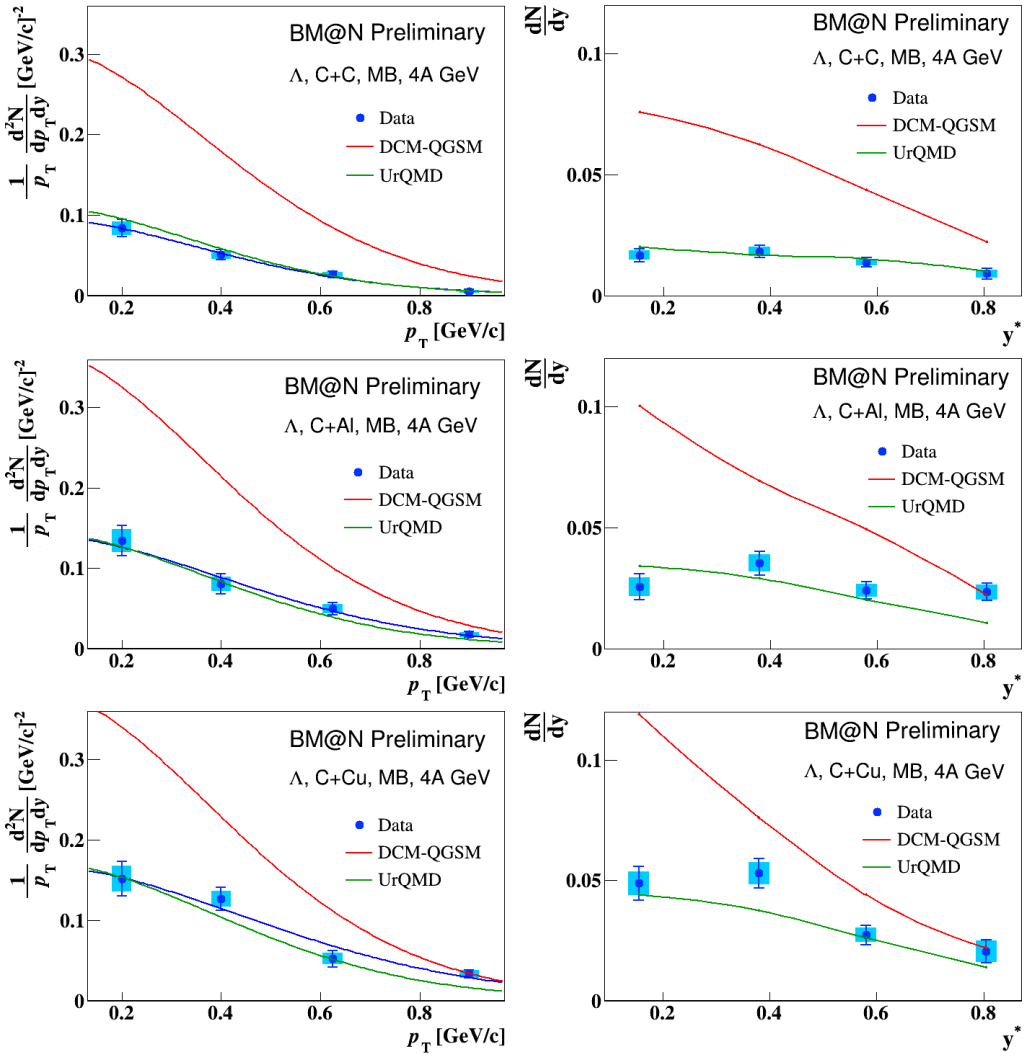

Figure 3.2.1.6 Yields of Λ hyperons in minimum bias C+C, C+Al, C+Cu interactions vs rapidity y^* in c.m.s. (left plots) and transverse momentum p_T (right plots). The error bars represent the statistical uncertainties, the blue boxes show the systematic errors. The predictions of the DCM-QGSM and UrQMD models are shown as colored lines.

A rise of the Λ yield per nucleus collision with the collision energy could be understood within the hadron cascade model as being due to a rising energy available for production of pairs of Λ and kaons in multi-scattering processes in interacting nuclei.

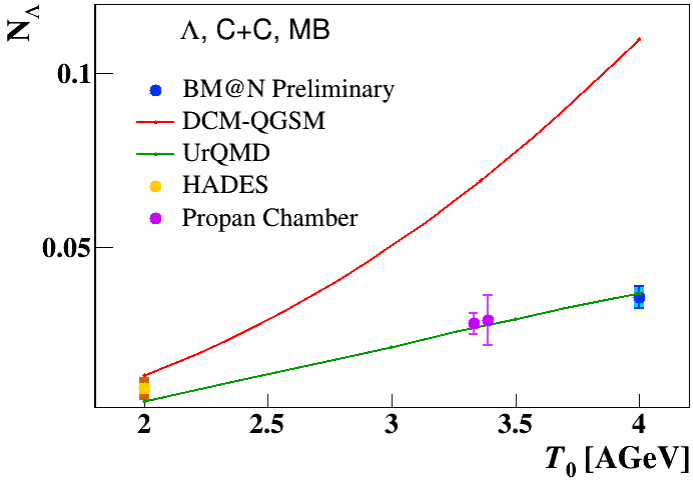

Figure 3.2.1.6 Energy dependence of Λ hyperon yields in C+C interactions. The BM@N result is compared with results of other experiments [3.2.16–3.2.18]. The BM@N error bar represents the statistical uncertainty, the blue box shows the systematic error. The predictions of the DCM-QGSM and UrQMD models are shown as colored lines.

In analogy with the analysis of the carbon beam data, Λ hyperons were reconstructed in argon-nucleus interactions using their decay mode into (p,π^-) pairs. Candidates to Λ decays were reconstructed as neutral V^0 topologies without identification of the decay products as it is shown in Fig.3.2.1.7(left). All positive tracks were considered as protons and all negative tracks as π^-. The invariant mass distribution of (p,π^-) pairs is shown in Fig. 3.2.1.7(right) for reconstructed interactions of the argon beam with fixed targets. The Λ hyperon signal has a width sigma of 3-3.5 MeV for different targets, which is similar to the width of the Λ signal in carbon-nucleus interactions. Taking into account the momentum spectra of reconstructed p, π^- decay products, the 3-3.5 MeV Λ mass resolution corresponds to 2.5-3.5% momentum resolution for p, π^-.

Charged kaons and pions, as well as protons and light nuclear fragments, were identified in the experimental data obtained in interactions of the 3.2 AGeV argon ion beam with fixed targets (C,Al,Cu,Sn,Pb) using the central tracking system (measuring the particle momentum and trajectory in the coordinate silicon detectors and GEM detectors) and the time-of-flight system of ToF-400 and ToF-700 based on the mRPC detectors (chambers) measuring the time of flight of charged particles from the starting T0 detector to the mRPC chambers. The particle velocity is determined from the length of the particle trajectory from the target to the mRPC chambers and the time of flight. Knowing the momentum and velocity of particles allows us to determine the mass and identify the particle. To improve reconstruction of the particle momentum, the detector alignment was performed, i.e. the positions and rotations of the silicon coordinate detectors and GEM detectors were determined by software methods.

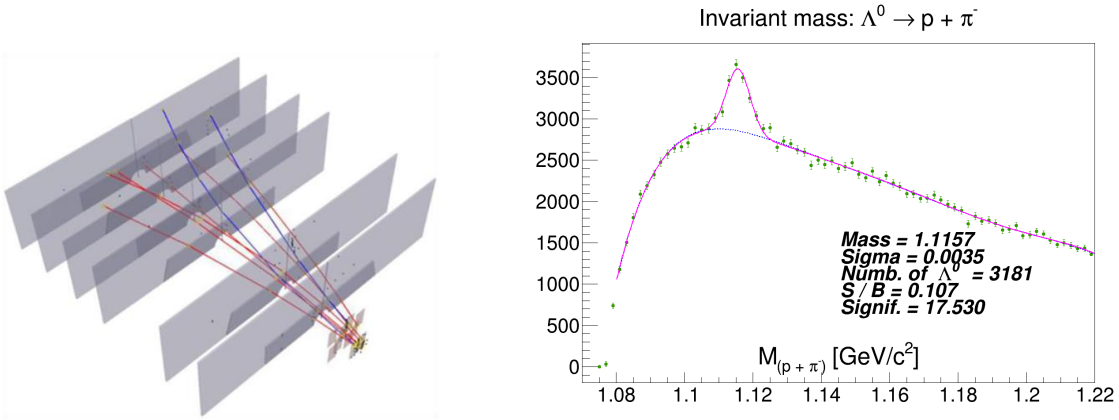

Figure 3.2.1.7 Left plot: Event of Λ hyperon production in a argon-nucleus interaction reconstructed in the central tracker. Right plot: Λ hyperon signal in the invariant mass spectrum of (p, π^-) pairs reconstructed in interactions of the 3.2 AGeV argon beam with the fixed targets.

To improve the time-of-flight measurement the response of the time-of-flight detectors T0 and mRPC was calibrated: the raw time-of-flight was corrected for the channel-by-channel time offset, for the propagation time in the MRPC strip, and for the correlation of the time measurement with the signal amplitude. The final tuning of the time-of-flight for individual mRPC chambers was performed using a large statistical sample of identified protons: the mean time-offlight measured in a chamber was adjusted to put the mean value of the mass of particles identified in the chamber as protons to the tabular value of the proton mass. The achieved time resolution of the ToF-400 and ToF-700 systems was 85 ps and 120 ps, respectively.

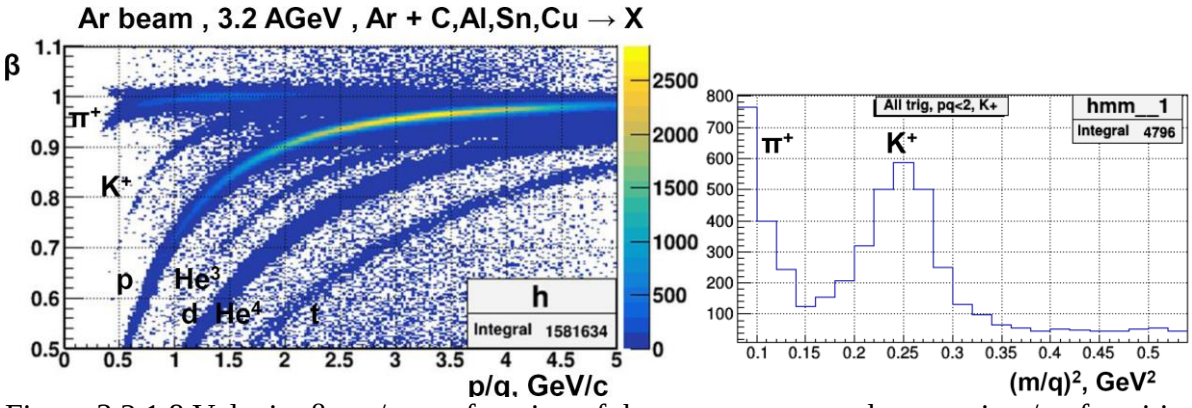

Figure 3.2.1.8 Velocity β = v/c as a function of the momentum-to-charge ratio p/q of positive charged particles measured in the ToF-400 system. Identified π^+, K^+, p, He^3 , d/He^4 , t are visible as populated bands of particles (left plot). Distribution of the squared mass-to-charge ratio of identified particles showing peaks of π^+ and K^+ (right plot).

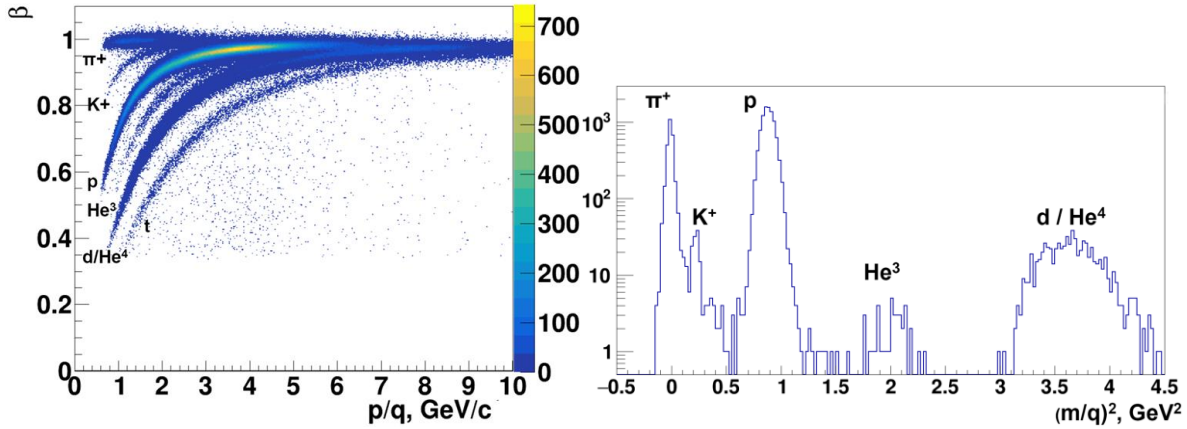

Figure 3.2.1.9 Velocity β = v/c as a function of the momentum-to-charge ratio p/q of positive charged particles measured in ToF-700 system. Identified π^+, K^+, p, He^3 , d/He^4 , t are visible as populated bands of particles (left plot). Distribution of the squared mass-to-charge ratio of identified particles showing the π^+, K^+, p peaks and light fragments (right plot).

The coordinate resolution of the mRPC detectors along the readout strips is 0.75 cm. Within the framework of the project, response of the time-of-flight detectors was simulated, and an algorithm for identifying particles in multiparticle events was developed. The results of particle identification in the ToF-400 and ToF-700 detectors are shown in Fig. 3.2.1.8 and Fig. 3.2.1.9, respectively. The populated bands of particles at the left plots and the peaks in the mass distributions at the right plots correspond to identified π^+, K^+, p, He^3, d/He^4 , t. In particular, the distributions of the squared mass-to-charge ratio of identified particles show the π^+ peak at low values of $(M/q)^2$ and the K^+ peak at ~0.25 GeV^2 (right plots). The analysis is going on to correct the identified data for the detector acceptance and efficiencies and extract the yields of $\pi^{\pm}$, $K^{\pm}$ mesons, Λ hyperons and light nuclear fragments in argon-nucleus interactions.

3.2.2 Simulation of the central tracker for the heavy ion program

The layout of the upgraded BM@N configuration for heavy ion program is shown in Fig. 3.1.1. At the first stage of the experiment starting in 2022, three planes of the forward silicon detectors will be used in combination with seven stations of the GEM detectors to reconstruct interactions of middle size ions (Kr,Xe) with fixed targets (see Fig.3.1.2). After 2023, at the final stage of the experiment, four planes of the large aperture two-coordinate silicon tracking system STS will be installed in front of the GEM detectors to improve track reconstruction in heavy ion collisions (see Fig.3.1.3).

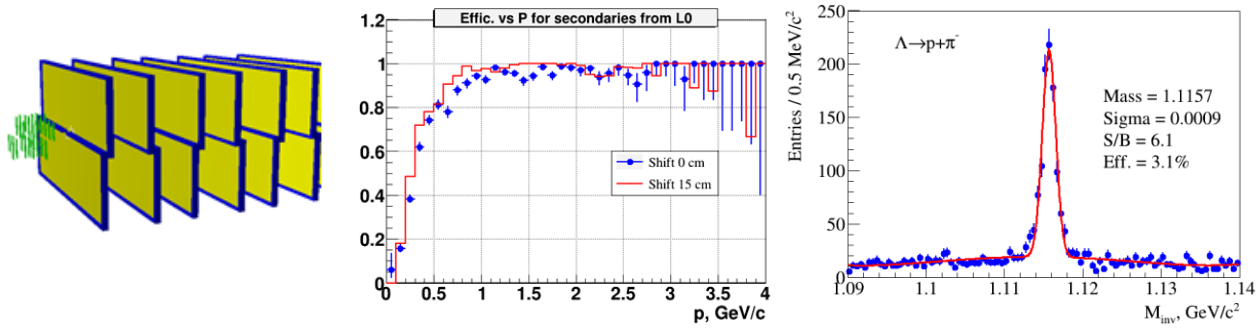

Figure 3.2.2.1 Left plot: Simulated configuration of the first stage of the hybrid tracker based on 3 FwdSi planes and 7 GEM detector planes. Central plot: Efficiency of the Λ decay product (proton or π^-) reconstruction in the hybrid FwdSi+GEM tracker in simulated Kr+Pb interactions. Right plot: Signal of Λ hyperon in the invariant mass spectrum of simulated (p, π^-) reconstructed in the hybrid FwdSi+GEM tracker.

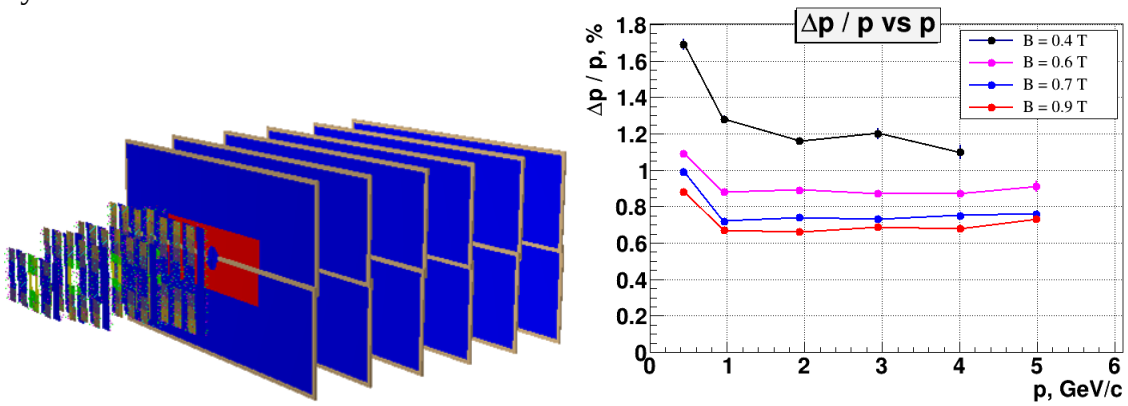

Figure 3.2.2.2 Left plot: Simulated configuration of the final stage of the hybrid tracker based on 4 STS stations and 7 GEM detector planes. Right plot: Momentum resolution of the hybrid tracker as a function of the particle momentum calculated for different values of the magnetic field.

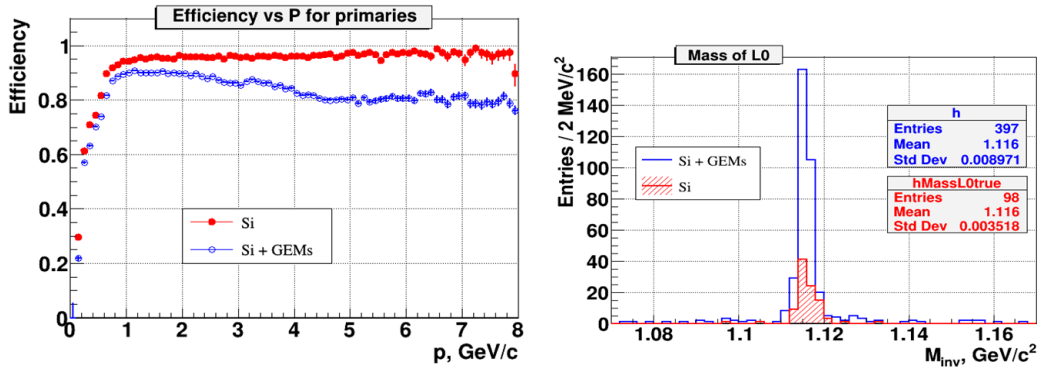

Figure 3.2.2.3 Left plot: Efficiency of primary charge particle reconstruction in the hybrid STS+GEM tracker (blue histogram) and STS tracker alone (red hystogram). Right plot: Reconstructed signal of Λ hyperon for the STS and STS+GEM tracker configurations.

The simulated configuration of the 1st stage of the hybrid tracker based on 3 forward silicon stations and 7 GEM detector planes (Fig.3.1.2) is shown in Fig. 3.2.2.1(left). The efficiency of the $\Lambda \rightarrow p + \pi^-$ decay product reconstruction in the hybrid FwdSi+GEM tracker in simulated interactions of the Kr beam with the Pb target is shown in Fig. 3.2.2.1(right). Results for two positions of the FwSi detectors are presented: default (Shift 0 cm) and shifted additionally at +15 cm from the interaction point.

Within the framework of the BM@N upgrade [3.2.20], the final configuration of the central tracking system based on the large aperture STS and GEM detectors (Fig.3.1.3) was simulated to study its performance for reconstruction of hyperons and hypernuclei in interactions of heavy

nuclei up to Au+Au (Fig.3.2.2.2left). As it is mentioned above, studies of Au+Au interactions are planned at the final stage of the BM@N experiment with heavy ion beams.

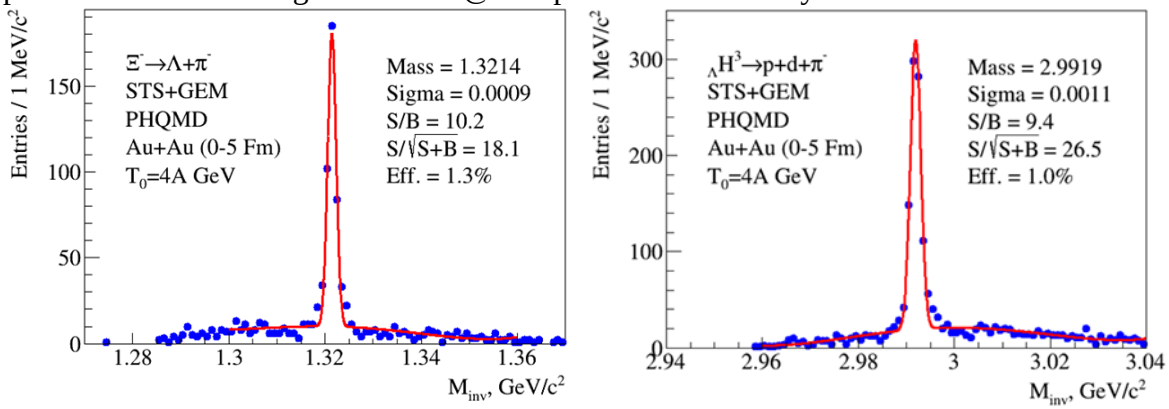

Figure 3.2.2.4 Left plot: Signal of Ξ^- hyperon in the invariant mass spectrum of simulated (Λ, π^-) reconstructed in the hybrid STS+GEM tracker. Right plot: Signal of ${}_{\Lambda}H^3$ in the invariant mass spectrum of simulated (p, d, π^-) reconstructed in the hybrid STS+GEM tracker.

The efficiency of reconstruction of primary charged particles in simulated central Au+Au collisions is presented in Fig. 3.2.2.2(central) for the hybrid STS+GEM tracking system (blue histogram) and for the silicon STS stations alone (red histogram). Although the GEM detectors are less efficient in high multiplicity events due to lower granularity than the STS detectors, the STS+GEM tracking algorithm is able to reconstruct four times more Λ hyperons than that of the STS tracker alone. The momentum resolution of the hybrid tracker is shown in Fig. 3.2.2.2(right). The hybrid tracking system is also able to reconstruct cascade decays of Ξ^- hyperons to $\Lambda+\pi^-$ and hypertriton nuclei ${}_{\Lambda}H^3$ in the decay modes to $He^3+\pi^-$ and $p+d+\pi^-$ with a similar efficiency. The Ξ^- and ${}_{\Lambda}H^3$ signals reconstructed in the STS+GEM tracking system are shown in Fig. 3.2.2.4. To reconstruct events with the Ξ^- or ${}_{\Lambda}H^3$ decay topolgies the algorithm developed at CBM [3.2.21] was used and the selection criteria were applied on the distance of the closest approach to the primary vertex of decay products, distance between tracks in the decay vertex, path length of the reconstructed mother particle. In addition, to reduce the combinatorial background under the ${}_{\Lambda}H^3$ signal in the decay modes to $He^3+\pi^-$ and $p+d+\pi^-$, the identification of He^3 and d was required in the ToF system. More details of the upgraded setup simulation could be found in [3.2.22].

Expected statistics of hyperons to be collected per second and for a quartal of data taking is given in the last two columns of the table below. We foresee 3-4 months of data taking per year.

Particle	E_{thr}NN GeV	M central	M m.bias	ε %	Yield/sec m. bias	Yield/quartal m. Bias
Ξ^-	3.7	$1\cdot10^{-1}$	$2.5\cdot10^{-2}$	1	2.5	$5\cdot10^{6}$
Ω^-	6.9	$2\cdot10^{-3}$	$5\cdot10^{-4}$	1	$5\cdot10^{-2}$	$1\cdot10^{5}$
Anti-Λ	7.1	$2\cdot10^{-4}$	$5\cdot10^{-5}$	3	$1.5\cdot10^{-2}$	$3\cdot10^{4}$
Ξ^+	9.0	$6\cdot10^{-5}$	$1.5\cdot10^{-5}$	1	$1.5\cdot10^{-3}$	$3\cdot10^{3}$
Ω^+	12.7	$1\cdot10^{-5}$	$2.5\cdot10^{-6}$	1	$2.5\cdot10^{-4}$	$5\cdot10^{2}$

In the table M(central) and M (m.bias) are the yields of hyperons per central / min bias event in Au+Au interactions at the kinetic beam energy of 4 AGeV predicted by the statistical model [2.17], ε is the estimated hyperon reconstruction efficiency, $E_{thr}NN$ is the kinematical threshold for the hyperon production. The DAQ event rate is assumed 10^4 Hz and the accelerator duty factor is taken as 0.25. Taking the statistical model predictions for hypernuclei yields per event and 1% reconstruction efficiency, the expected yields of hypernuclei ${}_{\Lambda}H^3$ and ${}_{\Lambda\Lambda}H^5$ for a quartal of data taking are 10^6 and 100, respectively.

References

[3.2.1] J. Steinheimer et al., Progress in Particle and Nuclear Physics 62, 313317 (2009).
[3.2.2] J. Steinheimer, K. Gudima, A. Botvina, I. Mishustin, M. Bleicher, H. Stocker, Phys. Lett. B 714, 85 (2012).
[3.2.3] NICA White Paper.
http://theor0.jinr.ru/twiki-cgi/view/NICA/NICAWhitePaper
[3.2.4] BM@N Conceptual Design Report:
http://nica.jinr.ru/files/BM@N/BMN CDR.pdf
[3.2.5] D. Suvarieva et al., J.Phys.Conf.Ser. 668 (2016) no.1, 012121.
[3.2.6] V. Friese, Strangeness Prospects with the CBM Experiment, talk at the SQM-2015 Conference, Dubna, Russia, July 6-11, 2015.
[3.2.7] D. Baranov et al., JINST 12 (2017) no.06, C06041.
[3.2.8] M. Kapishin (for the BM@N Collaboration), Eur.Phys.J. A52 (2016) no.8, 213.
[3.2.9] M. Kapishin (for the BM@N Collaboration), Phys.Atom.Nucl. 80 (2017) no.10, 1613-1619, Yad.Fiz. 7 (2016) no.6, 543-550.
[3.2.10] M. Kapishin (for the BM@N Collaboration), Nucl.Phys. A982 (2019) 967-970.
[3.2.11] M. Kapishin, Proceedings of the 13th International Conference on Nucleus-Nucleus Collisions (NN 2018), JPS Conference Proceedings, v.32 (2020), 010093
[3.2.12] M. Kapishin (for the BM@N Collaboration), The XVIII International Conference on Strangeness in Quark Matter (SQM 2019), Springer Proceedings in Physics, v.250 (2020), 21-27
[3.2.13] V. Akishina and I. Kisel, J. Phys.: Conf. Ser. 599, 012024 (2015), I. Kisel, Nucl. Instrum. Meth. A 566, 85 (2006).
[3.2.14] D. Baranov et al., Phys.Part.Nucl.Lett. 15 (2018) no.2, 148-156.
[3.2.15] N. Amelin, K. Gudima, and V. Toneev, Sov.J.Nucl. Phys. 51, 1093 (1990).
[3.2.16] S. Arakelian et al., P1-83-354, JINR, Dubna.
[3.2.17] D. Armutlijsky et al., P1-85-220, JINR, Dubna.
[3.2.18] K. Kanaki, Study of hyperon production in C+C collisions at 2A GeV beam energy with the HADES spectrometer, PhD 2007.
[3.2.19] F. Guber et al., Measurement of centrality in nucleus-nucleus collsions at the BM@N experiment, these proseedings.
[3.2.20] P. Senger, D. Dementev, J. Heuser, M. Kapishin, E. Lavrik, Yu. Murin, A. Maksymchuk, H.R. Schmidt, Ch. Schmidt, A. Senger and A. Zinchenko, Upgrading the Baryonic Matter at the Nuclotron Experiment at NICA for Studies of Dense Nuclear Matter, Particles, 2, 481 (2019).
[3.2.21] S. Gorbunov and I. Kisel, Reconstruction of decayed particles based on the Kalman filter, CBM-SOFT-note-2007-003 (2007).
[3.2.22] A. Zinchenko et al., Performance evaluation of the upgraded BM@N setup for the strangeness production studies, these Proseedings

3.3 Central tracker

3.3.1 GEM tracker

Central tracking system of the BM@N experiment should provide precise momentum measurements of the cascade decays products of multi-strange hyperons and hyper-nuclei produced

in central Au-Au collisions. All physics measurements will be performed in conditions of high beam intensities in collisions with large multiplicity of charged particles. This requires the use of detectors with the capacity to resolve multiple tracks produced at very high rate. The basic requirements for the tracking system are: capability of stable operation in conditions of high radiation loadings up to 10^5 Hz/cm^2, high spatial and momentum resolution, geometrical efficiency better than 95%, maximum possible geometrical acceptance within the BM@N experiment dimension, operation at a 0.8 T magnetic field. Detectors based on the GEM technology posses all the mentioned characteristics combined with the capability of stable operation in a strong magnetic field up to 1.5T.

BM@N GEM detectors.

Production and assembly processes of the large size (up to 2m long) GEM-based detectors are well developed at CERN PH DT and MPT Workshop. Since non-glue «foil-stretching» technology is involved, one chamber can be assembled in several hours and easily re-opened for technical service if needed. For this reason, two coordinate triple GEM detectors were chosen for the central part of the BM@N tracking system. Triple-GEM configuration performs low probability of discharge propagation and stable operation at gains above 10^5. BM@N GEM detectors consist of three multipliers, with a drift gap of 3 mm, first transfer gap of 2.5 mm, second transfer gap of 2 mm and an induction gap of 1.5 mm. Two-coordinate readout of the signal is done by the sets of parallel metal strips on the anode readout board. The inclination angles of bottom layer strips (X coordinate) and top layer strips (X′ (or Y) coordinate) to the vertical are 0 and 15 degree, respectively. X and X′ strip widths are 0.68 and 0.16 μm. The strip pitch is 800 μm for both layers. Groups of 128 strips are connected to the inputs of the front-end ASIC via a connector on the readout board. The transverse structure of the triple GEM detector and readout board design are shown in figure 3.3.1.

The BM@N GEM tracking system final configuration will consists of two types of the GEM chambers: 1632×450mm^2 and 1632×390 mm^2. In order not to be flooded by the primary non-interacting heavy ion beam particles and near halo there is a hole in the central region of the detector. Because of large multiplicity near the beam line, readout layer is divided into outer and inner (hot) zones for both types of detectors.

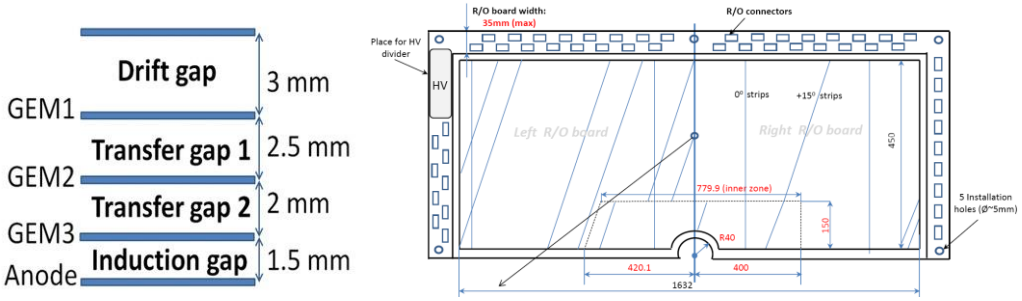

Figure 3.3.1. Left plot: Scematic transverse structure of the triple GEM detector. Right plot: Two-coordinate readout board of the 1632×450mm^2 GEM detector.

Figure 3.3.2. Left plot: GEM chambers integrated into BM@N experimental setup. Right plot: Cosmic ray test bench.

Beam tests of seven 1632×450mm^2 GEM chambers equipeed with VA163 based FEE were performed in 2018 with the argon and krypton beams (Fig. 3.3.2, left plot). The GEM detectors were filled with the flowed Ar(80)/C_4H_{10}(20) gas mixture to increase the avalanche electrons velocity. The tracks of charged particles were reconstructed and track detection efficiency of the GEM chambers was calculated (estimated average efficiency ~ 95%). Gaussian fit of hit residuals distribution gives standard deviation of 230 μm. Seven 1632×390 mm^2 GEM detectors have been assembled in 2019. Now the detectors equipped with electronics are under long-term measurements with cosmic rays (Fig. 3.3.2, right plot). Performance of the GEM detectors in the technical run with the deuteron beam is illustrated in Fig.3.3.2.1 and 3.3.2.2.

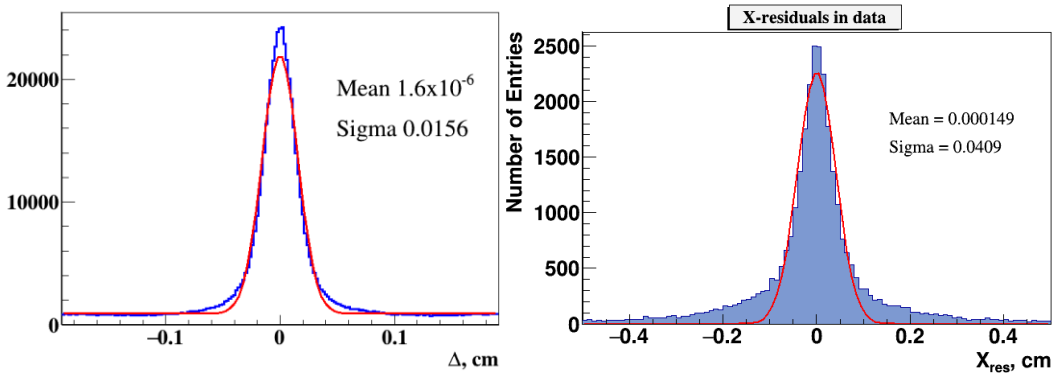

Fig.3.3.2.1 GEM hit to track residuals measured in beam-target interactions without magnetic field (left) and with magnetic field On (right).

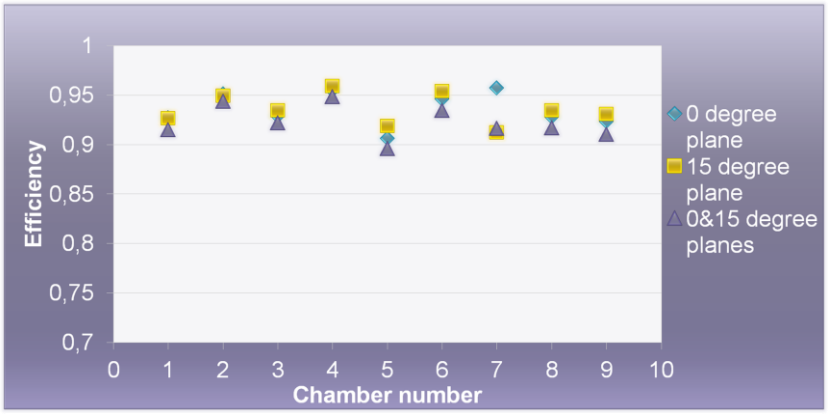

Fig. 3.3.2.2 GEM chamber efficiencies measured in the deuteron beam run.

Front-end electronics and DAQ system

For heavy ion program with the beam intensities up to few 10^5 Hz GEM front-end electronics is based on the charge sensitive pre-amplifier chip VA163(IDEAS, Norway). The chip has 32 channels. Each channel contains a charge-sensitive preamplifier, a shaper 0.5 μs peaking time and a sample-hold circuit. An analog multiplexer with 32 inputs allows one to perform serial read-out channel by channel. The chip can be used to amplify and read negative and positive charges in the range from -1.5 pC to +1.5 pC. The equivalent noise charge is 1900e without load, and 2000e at 50 pF input load. The integral linearity is 1% and 3% for positive and negative charge, respectively. Each read out card includes four chips, which are installed, bonded and filled with black compound. Thus, we have 128 input analog channels read-out board. The multiplexed data from each board are transmitted through 15 m of twisted pair flat cable to the 12-bit analog-to-digital converter readout by the BM@N data acquisition system.

For heavy ion program with the beam intensities up to few 10^6 Hz GEM electronics is to be upgraded. VMM3a and TIGER ASICs are considered as possible candidates. First tests of FEE based on both chips are already started. For VMM3a tests with BM@N GEM detectors Kintex7 based 128-channel evaluation board was designed and produced. Before 2023 new electronics will be developed.

Gas distribution system

GEM chambers can be operated with Ar(70)/CO_2(30), Ar(90)/C_4H_{10}(10), Ar(80)/C_4H_{10}(20) gas mixtures. The gas system consists of two parts: 1) the mixer system which delivers quantity, mixing ratio and pressure conditioning to downstream elements; 2) the distribution system, which delivers the gas in well defined quantities to the individual detectors. The gas system is produced by Ltd «Eltochpribor» (Zelenograd, Russia). To reduce oxygen and moisture impurities in GEM gas mixture, it will be distributed to detectors by seven independent gas lines, one for each GEM plane. Gas panel designed to control oxygen and moisture impurities in gas mixture is currently under development and will be based on GE oxy.IQ analyzers.

Integration into the BM@N setup

The final configuration of the central tracking system consists of 14 GEM detectors:

- 7 GEM detectors of the size 1632×450 mm^2 – above the vacuum beam pipe;
- 7 GEM detectors of the size 1632×390 mm^2 – below the vacuum beam pipe.

Since the magnetic field is perpendicular to the electric field direction inside the GEM chamber, electron avalanche in the gas gaps drifts at some angle (the Lorentz angle) with respect to the normal to the readout board. The electron cloud drift results in a displacement of the collected charge, which is called Lorentz shift. The shift value depends on the field strength and gas properties. To eliminate a systematic shift of the reconstructed tracks in the magnetic field, GEM detectors are oriented in alternating order so that the electric field for the neighboring planes has opposite directions. The full configuration with 14 GEM detectors (~90000 readout channels) is planned to be integrated in the BM@N experimental setup at the middle of 2021 with the electronics based on VA-163 chips.

The development of the mechanics design to provide GEM planes precise installation inside the magnet was performed by Ltd «Pelcom-Dubna» (Dubna, Russia) (see Fig. 3.3.6). The production of the mechanics will be performed till autumn 2021.

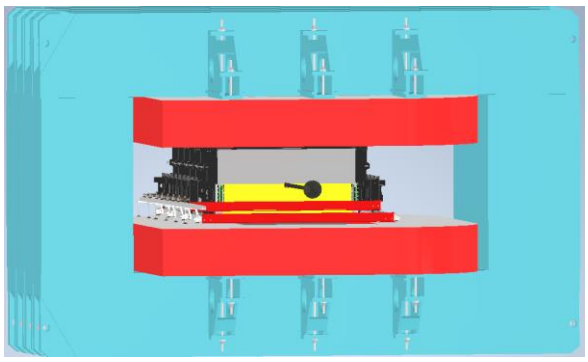

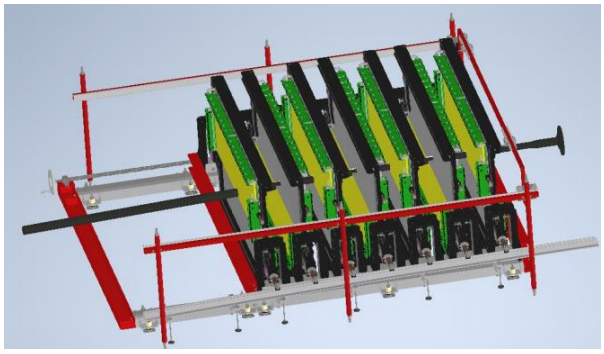

Fig. 3.3.6. A design of the mechanics for GEM planes precise installation inside SP-41 magnet

Material budget for the GEM central tracking system full configuration together with electronics and support mechanics was estimated (see Fig. 3.3.7).

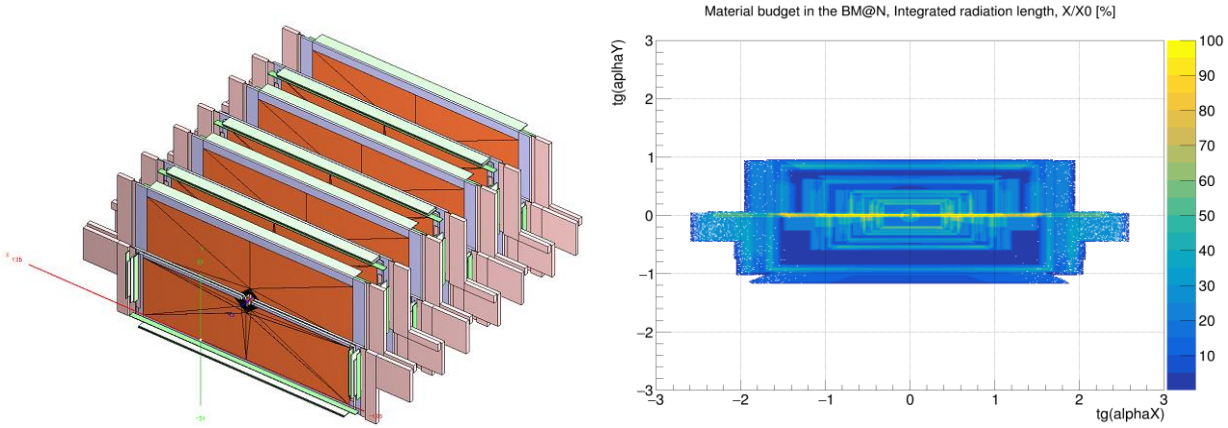

Fig. 3.3.7. Left panel: Detailed geometry of GEM planes for heavy ion beam run. Right panel: Material budget of the GEM central tracking system full configuration (angular distribution).

The GEM performance and characteristics are described in the TDR report [3.3.11].

3.3.2 Forward silicon detectors

Forward silicon detectors (FwdSi) are installed between the target and the GEM stations to increase the tracking efficiency and improve the precision of the primary vertex reconstruction. The results of simulation of the hybrid central tracking system based on the FwdSi and GEM detectors are presented in section 3.2.2. The schematic views of the silicon detector modules and the silicon detector planes are given in figure 3.3.8. Fast signals from readout chips of the segmented SiD trigger detector situated in front of the FwdSi detectors formes a trigger signal for multi-particle events (see section 3.7.2).

Design of the existing Forward Silicon Detectors

FwdSi detectors consist of three planes combined from two half planes (Fig. 3.3.8). Each half-plane has a hole for a beam pipe, inlet and outlet for the cooling system (cold dry air), and cross-boards for connection with the DAQ system and power supply. The details of the existing FwdSi detectors are described in document [3.3.12].

A silicon detector module consists of two DSSDs, which are wire bonded strip to strip. The detector sensitive volume is 63x63x0.3 mm^3. The pitch for the p^+ (n^+) side is 95 (103) μm. Stereo angle between strips is 2.5 degrees, number of strips for each side – 640. Since detector does not have integrated capacitors, Pitch Adapter (PA) is used to electrically decouple the DC current from the electronic inputs. PA has two different topologies for each DSSD side. Each PA has 640 channels. After PAs signal from detector transfer to VATAGP7.1 ASICs manufactured by IDEAS, Norway (5 chips per module side). The main ASIC parameters are 128 input channels, multiplexed output and dynamic range ± 30 fC.
The performance of the FwdSi detectors in the argon beam run is illustrated in Fig.3.3.9 showing residuals of Si hits to tracks. Tracks are reconstructed in a combined set of the FwdSi and GEM detectors.

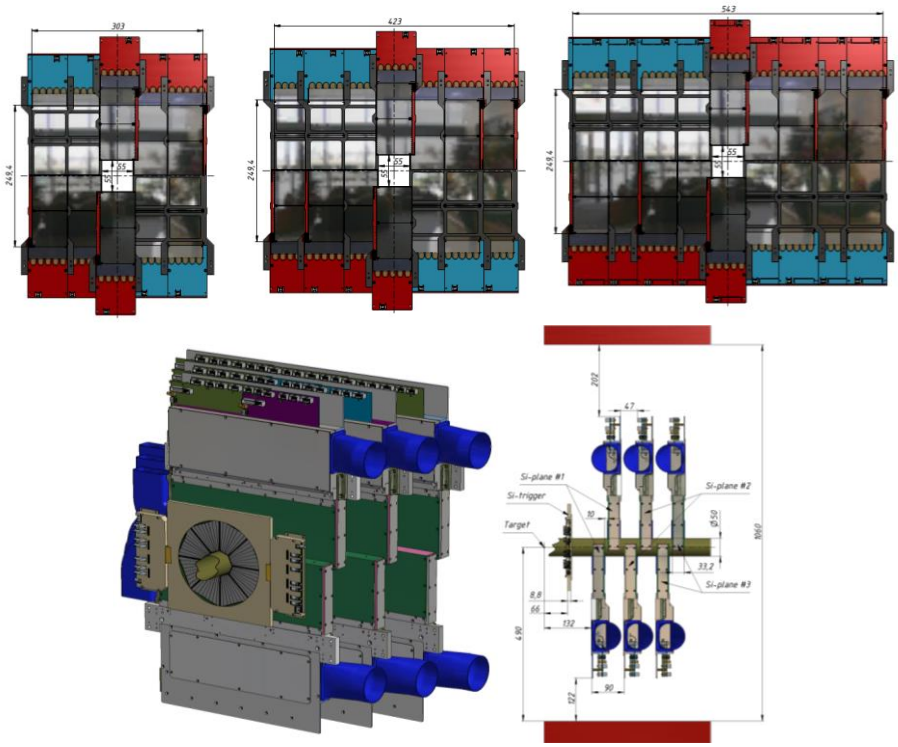

Figure 3.3.8. Schematic view of the silicon detector modules; combined view of the silicon detector plane**;** the prototype of the mechanical box for the silicon detector installation.

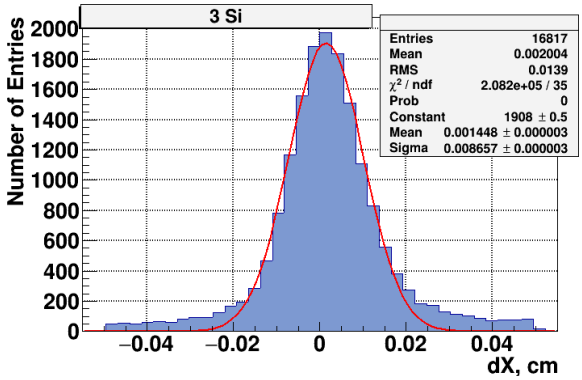

Fig.3.3.9 FwdSi hit to track residuals measured in the argon beam run.

An additional 4th plane of Forward Silicon Detectors will be designed to increase the track reconstruction efficiency and the acceptance of the existing FwdSi detectors. The new plane will consist of two half-planes with 11 large area (186x63 mm^2) silicon detector modules based on two DSSD with sensitive volume of 93x63x0.3 mm^3 (Fig. 3.3.10). Two DSSD are bonded strip to strip by wires. The pitch for the p^+ (n^+) side is 95 (103) μm. The stereo angle between strips is 2.5 degrees, the number of strips on each side is 640.

Forward Silicon Detector upgrade plan

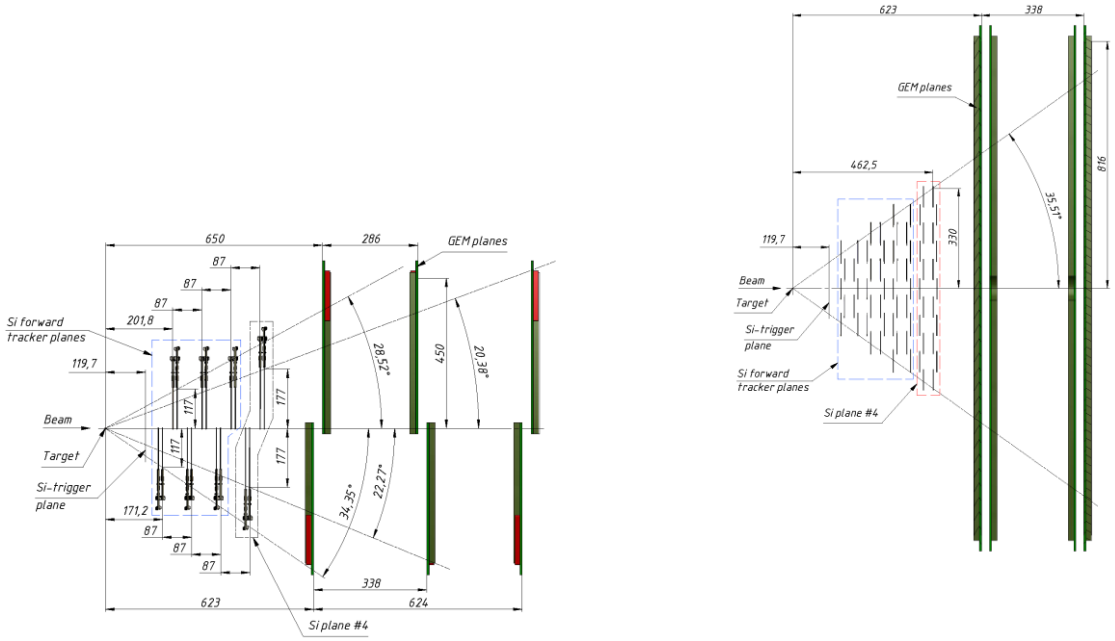

Figure 3.3.10. Schematic view of Forward Silicon detectors including 4th Si plane and first large apperture GEM stations in YZ (left) and XZ (right) projections.

The FEE design for the existing FwdSi detectors will be used. To increase the readout event rate capacity of the FwdSi tracker up to final 50 kHz, a FEE based on TIGER ASIC (INFN, Italy) is considered. The main chip parameters are: 64 input channels, shaping time of 60 and 170ns. The decision on usage of the TIGER ASIC for a new high rate FwdSi FEE will be done after the ongoing R&D. The total number of the FwdSi readout channels is 81920.

3.3.3 STS tracker

In 2022 BM@N experiment will be upgraded in order to fit occupancy challenge of Au+Au collisions with beam energies up to 4.5A GeV. A new hybrid tracking system based on four large aperture stations of double-sided microstrip silicon sensors of high granularity followed by 7 planes of two-coordinate GEM detectors and a vacuum beam pipe will be installed. Results of the physics performance simulations of the hybrid tracker are presented in [3.3.13]. Silicon planes are currently under development following the design used for the STS of the CBM experiment. The BM@N STS project will be performed in two steps: firstly, two stations with 44 modules will be assembled, installed and commissioned at the end of 2022, the full configuration will be ready in 2023-2024 provided priority given to the BM@N STS and not to the CBM STS project since they both share same module assembly line at VB LHEP.

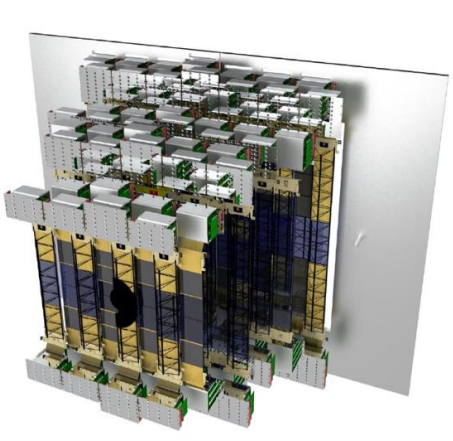

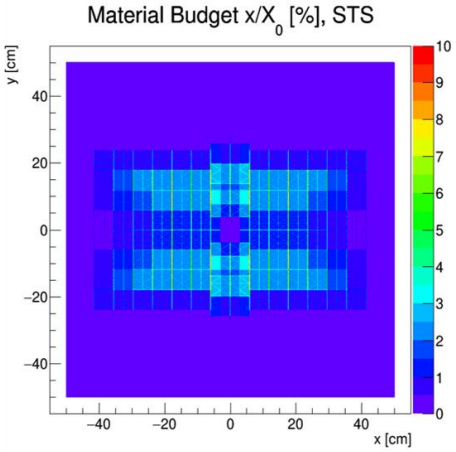

Fig. 3.3.3.1 Left panel: Layout of the BM@N STS detector. **Right panel**: space distribution of the total material budget for four STS stations.

The Silicon Tracking System (STS) of the BM@N consists of four stations equipped with 292 double-sided micro-strip silicon sensors providing information on the position, time and energy released by the particle passing through a sensor of the STS. The STS configuration is described in details in [3.3.14]. STS sensors of two sizes are used: 42 mm x 62 mm, and 62 mm x 62 mm. The sensors have a thickness of 320 ±15 μm. Each sensor has 1024 strips on each side with a strip pitch of 58 μm. Strips on the N-side of the sensor are straight, while the strips on the P-side are titled at an angle of 7.5° relative to the strips on the opposite side. Consequently, the minimum sensitive area of the sensor for a two-coordinate spatial measurement, i.e. a "pixel" has a size of $\Delta x = 58$ μm times $\Delta y = 58$ μm/tan(7.5°) = 440.6 μm. Short angled strips located on both edges are connected via a second metallization layer on the P-side.

The 2048 strips of each sensor (P and N side) are readout simultaneously by 16 ASICs sitting on 2 Front-End Boards (FEBs). Each ASIC is connected to the sensor via 2 low-mass aluminum-polyimide micro-cables, each reading out 64 strips. These cables, which vary in length between about 15 and 35 cm depending on the position of the sensor and the size of the station, allow to locate the readout electronics at the periphery of the station. This is required for two reasons: Firstly, the material budget of the active detector area, and, hence, the scattering of the particles is strongly reduced. Secondly, the radiation sensitive circuits of the readout electronics are positioned in a region of much lower particle density. The unit consisting of a sensor, 32 cables and a FEB is called a *module*. Several modules are mounted on ultralight spaceframes, *the trusses*, made of high modulus carbon fiber. This super module, consisting of up to 10 modules with readout micro-cables transmitting the signals in both directions (up and down), is the so-called *ladder*. The stations 1, 2, 3, and 4 comprise 24, 52, 64, and 104 modules, respectively, with sensors of size 62x62mm². In the inner part of each station, 8 modules with sensors of size 42x62mm^2 are located. Four modules with *central sensors* of size 42x62mm² with cut edges cover the space close to the beam pipe, in order to detect the particles emitted at the smallest scattering angles.

The layout of the STS is shown in the left panel of Fig.3.3.3.1. The first station is located 30 cm downstream the target. The distance between all STS stations is 20 cm. The sensors on the ladders are tiled with an overlap of 1,3 mm to cover the existing 1 mm wide dead area at the edges of the sensors. The ladders in the center of the stations form a semicircle opening which will finally, when all stations are installed in a mainframe, form a bore in the STS for the placement of the vacuum carbon fiber beam pipe transporting the incident beam through the STS to the beam dump. The space distribution of the material budget for all STS stations is shown in the right panel of Fig.3.3.3.1. The total material budget does not exceed 10% of X0, while the average value is ~3% of X0.

Radiation calculations

The radiation calculations were performed with FLUKA assuming a gold beam with energy 4.5 AGeV, a profile with σ=3.5 mm and a divergence of 1 mrad and intensity 2 MHz. In the simulations, the beam permeates the setup in a vacuum thin-wall beam pipe with the walls made of carbon fiber. Simulations have shown, that in the region of STS the total ionizing dose for the whole lifetime of the experiment will reach 100 Gy. The equivalent neutron fluence for the same period will be 10^{11} n_{eq}/cm^2. Both values are well within the radiation tolerance of the sensors.

STS Modules

The key component of the STS is a module. Each sensor has 1024 strips on both sides. They are connected to the readout ASICs via low-mass aluminum-polyimide micro-cables. A total of 8 STS-XYTER ASIC are needed to carry out signals from one side of the sensor. ASICs are installed on the Front-End Boards (FEBs) that are equipped with specially developed LDOs with a low noise density. The main constrain of the module is its very tight layout. Strips on the sensor have a pitch of 58 μm and for the readout of the analog signals, micro-cables with a 100 μm pitch of signal lines

were developed. The assembling of the module comprises TAB-, die- and wire-bonding procedures, as well as alignment and gluing steps described in [3.3.14]. Bonding procedures are performed with a help of ultrasonic bonding machines F&K Delvotec G5. A photo of the assembly procedure as well as bonding test procedure is shown in Fig. 3.3.3.4.

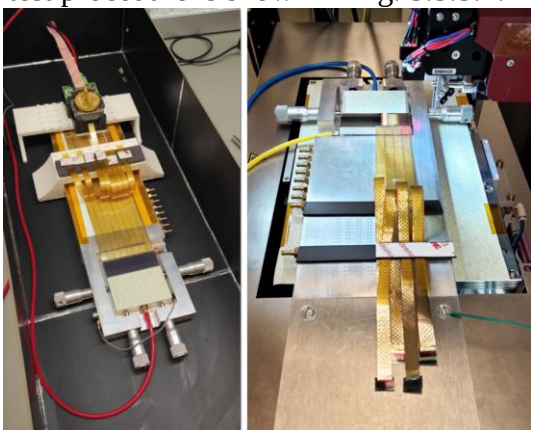

Fig. 3.3.3.4 Left: Photo of the bonding test procedure, which is performed after each step of the assembly. **Right:** TAB-bonding of the micro-cables to the sensor.

Ladder assembly

The ladder is a “super-module” of the STS. It consists of several modules attached to the ultra-light carbon-fiber spaceframe. Each spaceframe has a custom-designed bearing on both sides. The bearings provide a precise positioning of the ladder on the mechanical support frame with an experimentally tested accuracy of ~2 μm in the directions across the beam line. Precise positioning is guaranteed by the system with ruby ball pins on the ladder support frame, and a customized reply part of the ladder positioning units glued to the edges of the carbon-fiber spaceframe to which the sensors are glued with the help of tiny L-legs made of fiberglass. The FEBs, two for each module, are placed inside the aluminum FEB-boxes, located on both sides of the ladder. The FEB-box provides a thermal interface between readout electronics and the heat exchanger plate. The layout of the BM@N ladder is shown in Fig.3.3.3.5.

The central part of the ladder comprises the sensors installed on the light CF frame. The frontend electronics is located on the both sides of the frame in aluminum FEB boxes. The assembly of the ladder is a delicate procedure, which requires a precise positioning of the modules. For that reason, a special Ladder Assembly Device (LAD) was developed. The LAD with a customized set of fixtures was produced at PLANAR, Ltd. Enterprise (Minsk) and installed at JINR in the end of 2019. It is equipped with an optical system for monitoring the sensor position in a horizontal plane with an accuracy of ±2μm. For the alignment of the sensors it comprises different sets of sensor-positioning vacuum chucks with micro-screws and a lift unit for the vertical displacement of the ladder sensor supporting carbon-fiber spaceframe. The LAD is installed on a heavy diabase table to avoid vibrations during its operation. The LAD provides an accuracy of sensor positioning of less than 15 μm across the ladder on the 1200 mm base.

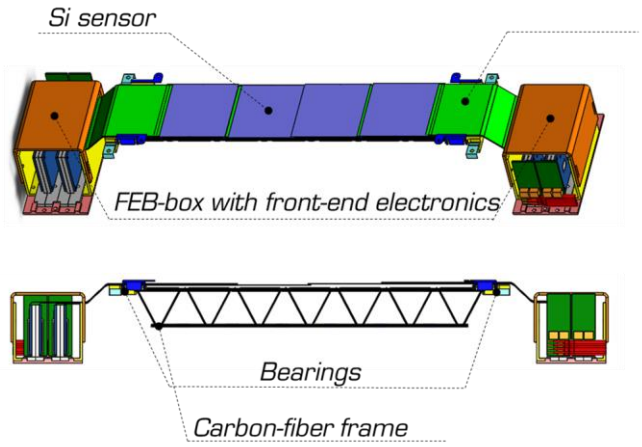

Fig.3.3.3.5*. Layout of BM@N ladder.*

Readout electronics of BM@N STS

The data acquisition chain of the BM@N STS conceptually exploits the free-streaming readout scheme being developed for the CBM. The frontend electronics of the STS is an integral part of the module that relies on the STS-XYTER ASIC developed by the CBM collaboration. Each ASIC provides 128 channels operating in a self-triggered mode. The ASIC provides a 5 bits amplitude and 14 bits time stamp information for each hit frame. The ASICs communicate with the system through the configurable multichannel e-link protocol. The maximum hit rate per one channel in the BM@N STS setup is ~20 kHz/channel. To provide a bi-directional optical link between the front-end electronics and data-processing units GBTxEMU boards are used. The GBTxEMU boards are equipped with Artix-7 FPGA produced by XILINX. Each board hosts firmware emulating the functionality of CERN GBTx ASIC.

Data processing is performed on the level of GBTxEMU Readout Interface (GERI) boards. These boards play a role of the back-end optical interfaces for the GBTxEMUs, and are equipped with a Virtex-7 FPGA from Xilinx. The data are sorted on the time-base and trigger decision, and are further transmitted to the global BM@N DAQ system.

References:

[3.3.11] http://bmnshift.jinr.ru/wiki/lib/exe/fetch.php?media=tdr_gem_may2017_v1.doc

[3.3.12] http://bmnshift.jinr.ru/wiki/lib/exe/fetch.php?media=forward_silicon_for_tdr.doc

[3.3.13] Senger P., Dementev D., Heuser J., Kapishin M., Lavrik E., Murin Y., Maksymchuk A., Schmidt H.R., Schmidt C., Senger A., Zinchenko A. Upgrading the Baryonic Matter at the Nuclotron Experiment at NICA for Studies of Dense Nuclear Matter // Particles 2019, 2. p.481-490

[3.3.14] A. Baranov et. al. (The BM@N STS group) The Silicon Tracking System as Part of the Hybrid Tracker of the BM@N Experiment: Technical Design Report // Dubna: JINR, 2020. 101 p.

3.4 Outer tracker

The purpose of the outer tracker is to provide link between tracks measured in the central tracker and hits in the ToF-400 and ToF-700 detectors. Initially it consisted of two large aperture drift chambers. Every drift chamber (DCH) consists of 4 double coordinate planes with the following parameters: the wire inclination angles of 0, 90, ±45°, the wire pitch of 10 mm, the outer dimentions of the sensitive area of Y_{out} ± 1.2 m, X_{out} ± 1.2 m, the beam hole radius of R_{min} = 10 cm, 256 wires per coordinate plane, 2048 wires per chamber. The granularity of DCH is sufficient to perform measurements of interactions with light ions (up to Ar). The DCH wire occupancy in interactions of middle and heavy nuclei is too high to perform efficient track separation. Thus, the DCH will be replaced by cathode strip chambers to perform track measurements in middle and heavy nucleus collisions.

3.4.1 Cathode Strip chambers

The full configuration of the outer tracking system for heavy ion program will consist of four planes of 1129×1065 mm^2 CSC (cathode strip chamber) and two planes of 2190×1453 mm^2 CSC. The CSC detectors are situated outside the magnetic field with the aim to make precise link to the tracks, reconstructed in the GEM detectors inside the analyzing magnet. Tracks refined in CSC are used to improve particles momentum reconstruction and to find corresponding hits in the time-of-flight systems ToF400 and ToF700.

The first CSC detector with the size of the active area of 1129×1065 mm^2 was designed and assembled at LHEP JINR in 2018. It consists of an anode plane located between two cathode planes (see Fig. 3.4.1a). The anode plane is a set of gilded tungsten wires with the diameter of 30 μm which are fixed on the plane with a step of 2.5 mm. The gap between the anode plane and each cathode plane is 3.8 mm. Two-coordinate readout of the signal is performed on two cathode PCB boards using sets of parallel metal strips. The inclination angles of the cathode strips to the vertical axis are 0 degrees (X coordinate) and 15 degrees (Y coordinate). The pitch of the X and Y strips is 2.5 mm. PCBs are glued to the support honeycomb. Due to a large multiplicity of charged particles in Au-Au collisions, readout layer is divided into outer (cold) and inner (hot) zones.

First beam tests of the 1129×1065 mm^2 CSC were performed in 2018 at the argon beam with kinetic energy of 3.2 AgeV and the krypton beam with kinetic energy of 2.3 AgeV at the Nuclotron. The CSC was installed upstream the ToF-400 time-of-flight detectors as it is shown in Fig. 3.4.1b. The main goal of the tests was to study the performance of the CSC detector and the FEE and readout electronics as a part of the BM@N experimental setup. The signal clusters were reconstructed as groups of adjacent strips with amplitudes of signals above the threshold. For the reconstructed clusters, the center of gravity, the width and the total charge were calculated. The average cluster width is 6 strips which is equal to 15 mm. The gap size between the anode and cathode is reduced to 3 mm instead of 3.8 mm in order to improve the spatial resolution in multitrack events.

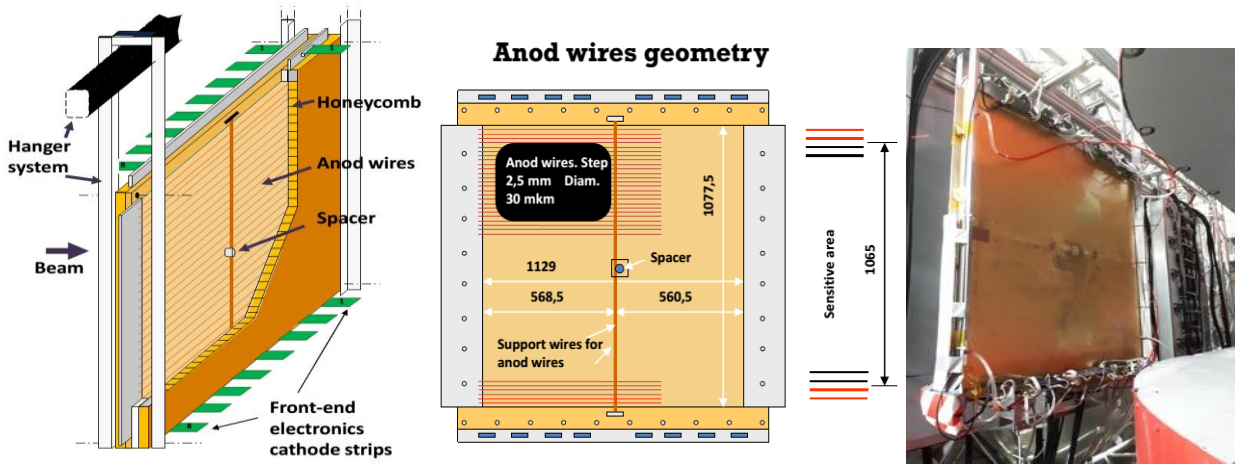

a) b)

Fig. 3.4.1 a) Schematic cross section of 1129×1065 mm^2 CSC b) 1129×1065 mm^2 CSC integrated into the BM@N experimental setup.

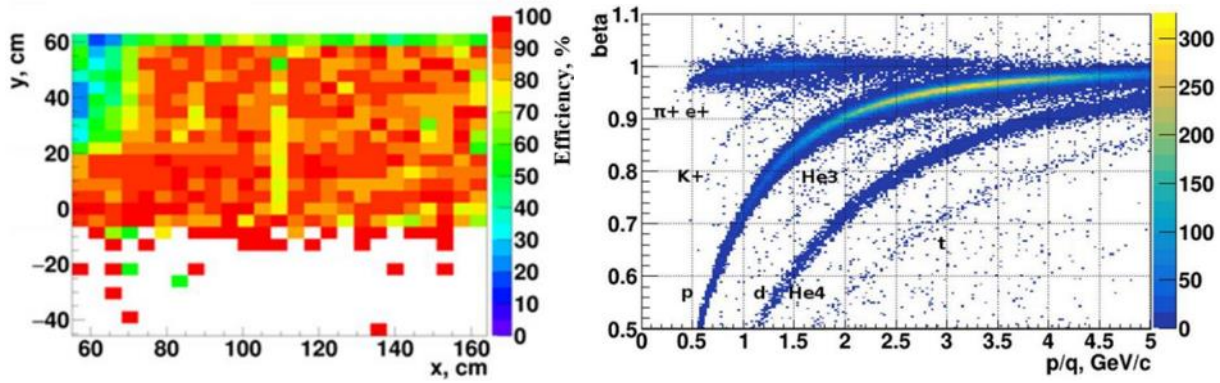

Fig. 3.4.2. Efficiency distribution for CSC (left); preliminary particle identification of GEM+CSC tracks extrapolated to the ToF-400 (right).

Tracks of charged particles were reconstructed in the GEM central tracking system and extrapolated into the CSC. The efficiency distribution over the chamber surface is presented in Fig. 3.4.2 (left). The efficiency for the area y < -5 cm was not estimated because of the relative location of the CSC and GEM detectors: the GEM detectors were covering the phase space only above the beam. The yellow vertical strip at x = 110 cm is an effect of the support wires. The green area at the left upper corner is due to a problematic front-end board. The combined tracks reconstructed from GEM and CSC hits were extrapolated to the TOF-400. Such procedure improves the momentum resolution and helps to separate secondary particles (π, p, K, light nuclei) in the momentum range 0.5-3.5 GeV/c (see Fig. 3.4.2, right).

All components for the assembly of three 1129×1065 mm^2 CSCs are delivered to JINR. The assembly process of three 1129×1065 mm^2 chambers is at the final stage. After passing quality assurance and cosmic tests three 1129×1065 mm^2 CSCs will be integrated into the BM@N setup in the middle of 2021.

Two CSCs of the size 2190×1453 mm^2 have been designed to cover the ToF-700 system on both sides and replace the existing DCH chambers. The design of these cathode strip chambers is shown in Fig. 3.4.3. One cathode plane consists of 8 PCBs, each PCB is divided into hot and cold zones. The hole in the center of the chamber is designed for the vacuum beam pipe. The gap size between the anode and cathodes is planned to be 3 mm. Two-coordinate readout of the signal is performed using sets of parallel metal strips with the inclination angle of 0 degrees for the X coordinate and 15 degrees for the Y coordinate. The pitch of the X and Y strips is 2.5 mm.

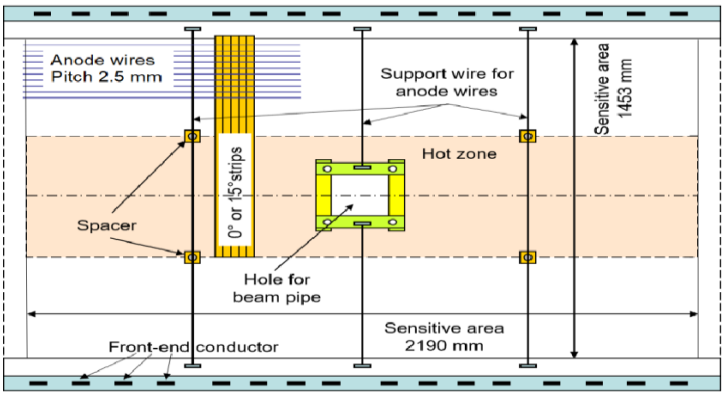

Fig. 3.4.3 A technical drawing of the cathode strip chamber of the size 2190 × 1453 mm^2 (15-degree strips are not shown in this picture).

The design of the 2190×1453 mm^2 CSC cathode planes was developed and VBLHEP JINR. The production was performed by "Mettatron group". The technological equipment for the assembly is under development. The assembly process of the first 2190×1453 mm^2 CSC is planned to be finished by the end of 2021 and of the second one – in the middle of 2022.

Front-end electronics

Front-end electronics is based on the same charge sensitive pre-amplifier chip VA163 as used for the GEM detectors (section 3.3.1). The multiplexed data from each board are transmitted through the twisted pair flat cable to the 12-bit analog-to-digital converter (ADC) readout by the BM@N data acquisition system. To improve the performance of the FEE, two new ASICs (VMM3a and TIGER) with the capability to measure both time and amplitude information are considered. First tests of FEE based on both chips have already started. In 2023 the new FEE electronics is planned be integrated into the BM@N experimental setup.

Gas distribution system

The CSC chambers can be operated with Ar(50)/CO_2(50) / C_3H_8O (vapour), Ar(75)/C_4H_{10}(25) / C_3H_8O (vapor) gas mixtures. The gas system consists of two parts: 1) the mixer system which delivers a mixture of gases in a required ratio and pressure to downstream elements; 2) the distribution system, which delivers the gas in well defined quantities to the individual detectors. The gas system is produced by Ltd «Eltochpribor» (Zelenograd, Russia).

Integration into the BM@N setup

The full configuration with 6 CSC detectors equipped with the electronics based on VA-163 chips (~35000 readout channels) is planned to be integrated into the BM@N experimental setup at the end of 2022. The upgrade of the CSC FEE is planned on 2023.

3.5 ToF system

The time-of-flight (ToF) system is based on the start time T0 detector installed near to the target and two walls of multi-gap resistive plate chambers (mRPC-1,2) sitated at distances of around 4 m and 7 m from the target as it is illustrated in figure 3.1.1. The time resolution of the ToF system of 80-100 ps is sufficient to discriminate between hadrons (π,K,p) as well as light nuclei with the momentum up to few GeV/c produced in multi-particle events. Figure 3.5.1 illustrates the resolution of the π/K separation by the ToF detectors and the geometrical acceptance of the mRPC-1,2 walls ToF-400 and ToF-700.

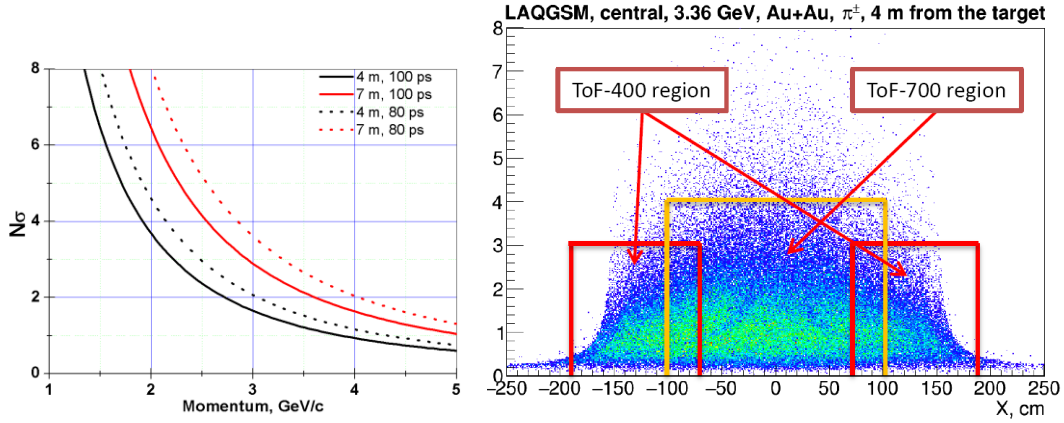

Figure 3.5.1. Left plot: resolution of the π/K separation presented as a function of the particle momentum for two values of the ToF system time resolution and for two distances between T0 and mRPC detectors. Rght plot: geometrical acceptance of the ToF-400 and ToF-700 mRPC walls for detection of charged pions produced in central Au+Au collisions.

3.5.1 Start detector T0

The details of the T0 detector design, the start time measuremnts in beams of light nucleus and heavy nucleus and the measured time resolution are described in section 3.7.1 and in the document [3.7.1].

3.5.2 ToF-400 mRPC detector

The details of the ToF-400 system and the technical parameters of the mRPC's are described in the document [3.5.1]. The schematic layout and the position of the ToF-400 wall are shown in figure 3.5.2. The time resolution of the integrated TOF400+T0 system of 85 ps is reached during BM@N Ar+Kr run. Pion/kaon separation is clear in the momentum range up to 2 GeV/c (see Fig.3.2.1.8). All subsystems work well, but we plane specific upgrade to get best performance of the TOF400.

Electronics for ToF-400

The DAQ electronics TDC72VHL are based on HPTDC hip. We plan to modify this modules to reach trigger data rate of 50 kHz. VXS synchronization system by backplane of VME crate should decrease dead time up to 1-2 mks and reduce readout errors. All TDC boards (27 pcs + 10 pcs reserve) are produced in 2017 and will be modified during 2021. It will be the same TDCs with additional back connector and new FPGA program.

Service systems

The mRPC works with a non-flammable Freon-rich gas mixture containing 90% C2H2F4 + 5% i-C4H10 + 5% SF6. The simple open gas loop system base on MKS mass flow meters are used. Flows are monitored by a process control computer which continuously calculates and adjusts the mixture percentages supplied to the TOF. The flow of the gas mixture can be adjusted in the range from 6 l/hour up to 90 l/hour. The same system is also used for ToF-700. We plan to produce new distribution module for divide gas flow between TOF400 and TOF700 systems. All main equipment for upgrade is purchased in 2020. We monitor several parameters as temperature, voltage, current, gas flow and etc for control the Time-of-Flight system of the BM@N. The slow control system has been developed. The data of the slow control system are used during experimental data analysis. All of the slow control equipment components are acquired in 2017.

Mechanical construction

The TOF-400 wall consists of two part (left and right) are placed symmetrical to the beam. Every part consist of two gas boxes (modules) which content 5 mRPCs each. Gas box made from aluminum frame covered by aluminum honeycomb for reduction of radiation length, but the edge of the gas box are still thick. The new design of gas box will be develop.

Gas boxes are installed on aluminum farm made from circular profile. This shape is not useful for CSC chambers which plan to be installed in 2021. New farm from Bosch profiles will be designed.

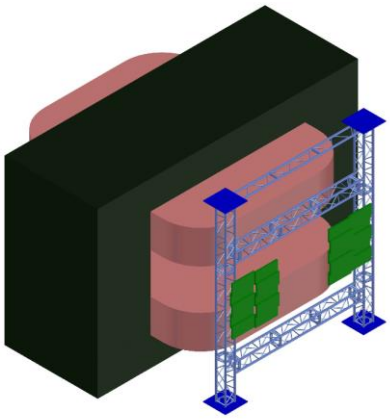

Fig. 3.5.2a Schematic layout of the ToF-400 mRPC wall and its position behind the analyzing magnet.

Fig. 3.5.2b Real view of a half part of the TOF400 system

3.5.3 ToF-700 mRPC detector

Time-of-flight detector ToF-700 placed at about 7m from the target provides BM@N with the pion/kaon separation up to 3 GeV/c and proton/kaon separation up to 5 GeV/c. ToF-700 system consist of 58 glass multigap Timing Resistive Plate Chambers (mRPC). The wall size of 3.2x1.6 m^2 is defined to satisfy the geometrical acceptance of the tracking detectors. Details of the ToF-700 mRPC detectors and the measured time resolution and efficiency are described in the TDR document [3.5.2].

Design of the ToF-700 wall

Conventional glass mRPC suffers from serious shortcomings – low hit rate capability. There are two ways to decrease the resistivity of "window" glass – to minimize its thickness or/and to heat the glass electrode. Our studies showed that the "warm" mRPC can provide us with good time resolution even at a rate of ~20 KHz/cm^2. Two types of mRPC were chosen for the construction of the wall plane: a "warm" mRPC for the central "hot" region with high rate of tracks, and a conventional "cold" mRPC for the "cold" region with low rate of tracks. An arrangement of 58 mRPCs in the wall plane is shown in Fig. 3.5.4. The hole in the wall center is for the beam pipe.

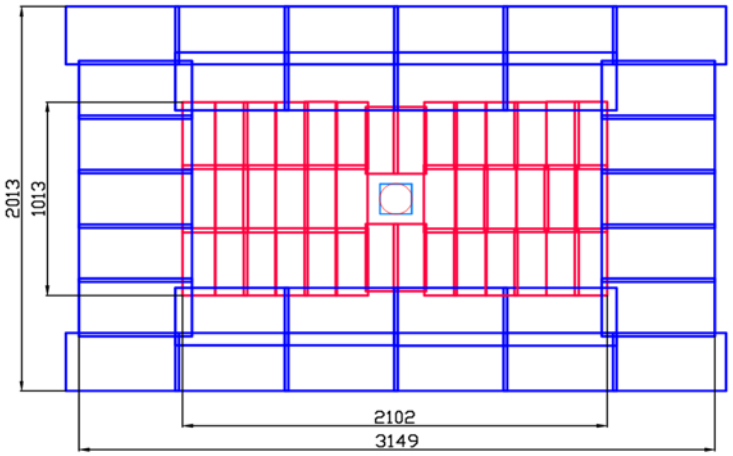

Fig. 3.5.4. Arrangement of 40 "warm" and 18 "cold" mRPCs on the wall plane.

mRPC's design and assembling

To optimize the number of chambers types and sizes, two types of mRPC were proposed: 18 "cold" mRPCs, each with the active area of 17.6x56 cm^2 (16 strips of 1x56 cm^2), for the region with the low hit rate and 40 "warm" mRPCs, each with the active area of 16 x 35.1 cm^2 (32 strips of 1x16 cm^2) for the region with the high hit rate and occupancy. The total number of chambers is 58, the number of strips - 1568. Each stack is formed by six glass plates with the bulk resistivity of $2x10^{12}$ Ω/cm. Signals are taken from both ends of the anode strips. The entire mRPC assembly is put into a gas-tight box.

Front-end electronics (FEE) of mRPC

A number of FEE channels for ToF-700 is 3136. As FEE for mRPCs readout the AddOn board developed for the HADES experiment was chosen. The 32-channels FEE module (32RPC board) designed for our mRPCs is based on the NINO chip. The output signal of the NINO amplifier-discriminator is the time-over-threshold pulse whose leading edge provides the time of the hit while its pulse width is proportional to the input signal charge. At present, a 64-channel VME time-to-digital converter TDC64VHLE based on the HPTDC chip is used for digitization.

The support of ToF-700 wall

To ensure an overlap between active areas of the mRPCs, the chambers should be arranged on the wall in four layers. The wall consists of two subwalls. The chambers are located on both sides of the sub walls. Both subwalls can move relative to each other to provide access for installation and maintenance.

ToF-700 data analysis

TOF-700 data analysis software was developed in the BMNROOT package framework. The analysis includes few stages and takes into account: INL (TDC non-linearity) corrections, VME crates Time Stamp differences, time corrections versus the T0 pulse width, time corrections versus the T0F pulse width, equalization of each strip time response for the main time peak. Finally, we use tracks reconstructed in GEM+DCH detectors and ToF-700 time data to reconstruct proton tracks and calculate the time correction for each strip (this correction shifts the reconstructed mass to the nominal proton mass). Fig. 3.2.1.9 illustrates the quality of the fragment separation versus the track momentum.

References

[3.5.1] http://bmnshift.jinr.ru/wiki/lib/exe/fetch.php?media=tdr_tof400_may2017_v1.docx
[3.5.2] http://bmnshift.jinr.ru/wiki/lib/exe/fetch.php?media=tdr_tof700_may2017_v1.docx

3.6 Calorimeters

3.6.1 Forward hadron calorimeter FHCal

A new forward hadron calorimeter (FHCal) will be served as a Zero Degree Calorimeter (ZDC) at the BM@N setup (Fig.3.1.1). It will be used to measure the centrality and reaction plane orientation in planned heavy ion experiments. In 2020 this calorimeter was completely assembled, including the installation of FEE boards with photodetectors in all calorimeter modules, as well as readout electronics. Photos of the calorimeter installed in the BM@N experimental hall on a mobile platform are shown in Fig. 3.6.1.

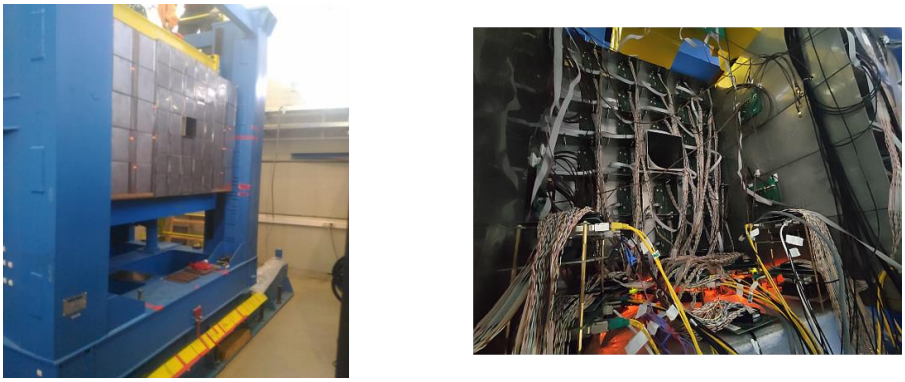

Figure 3.6.1. Photos of new FHCal calorimeter. Left, front view. Right, rear view of the calorimeter with electronics.

The already constructed calorimeter is positioned at the end of the BM@N setup at a distance 9 m from the target (see Figure 3.6.1, right). The calorimeter has modular structure in the transverse plane and consists of 54 individual modules. The inner part of FHCal consists of 34 modules with transverse sizes of 15 × 15 cm^2. There is the beam hole in the center with transverse size 15 x 15 cm^2. This hole is required to reduce the radiation dose and activation of the calorimeter and to reduce the neutron background at the rear part, where the photodetectors and electronics are located. The inner modules are identical to ones of the forward hadron calorimeters of the MPD experiment at the NICA accelerator complex and have a length equal to 4 nuclear interaction

lengths. The outer part consists of twenty modules with transverse dimensions of 20×20 cm^2 and a length equivalent to about 5.6 nuclear interaction lengths. The modules were initially constructed for the CBM hadron calorimeter at the FAIR accelerator complex and will be temporary used in the hadron calorimeter of the BM@N experiment until the commissioning of the CBM experiment. All FHCal modules have sampling structure. The CBM modules have 60 lead/scintillator layers, while the MPD/NICA modules have 42 similar layers. Each layer consists of 16 mm lead plates and 4 mm scintillator plates. The light from each scintillator plate is transported to the end of modules with WLS-fiber embedded in the groove in the plate. The fibers of each six consecutive scintillator tiles are combined to one optical connector and light from these 6 fibers is read-out with single photodetector (Hamamatsu MPPC with active sensitive area 3 x 3 mm^2) mounted on front-end electronics plate at the end of the module. Such longitudinal segmentation provides the uniformity of the light collection along the module and high dynamic range of the calorimeter response. The segmentation of modules also allows us to perform the FHCal energy calibration with cosmic muons. In 2020 the calorimeter was installed at the BM@N, equipped with FEE and readout electronics.. The installation and adjustment of the 54 FEE readout electronics boards were carried out. For data readout, a system of 8 ADC64s2 ADC boards was assembled. Each board can read up to 64 channels with differential input, all boards have been integrated into the common DAQ of the BM@N experiment. Commissioning and energy calibration of the FHCal with cosmic muons was started in 2021.

3.6.2 Fragment quartz hodoscope for FHCal

The presence of a beam hole in the calorimeter leads to a significant leakage of heavy fragments through this hole and, as a consequence, to a non-monotonic dependence of the deposited energy in the calorimeter on the collisions centrality. To solve this problem, it is proposed to use together with the FHCal a nuclear fragment hodoscope (FQH), which will measure the charges of heavy fragments. The FQH consist of 16 quartz plates 160 mm long, 4 mm thickness and 10 mm width. The active area of the hodoscope is 160x160 mm^2. The light from each of the 16 quartz plates is readout from two opposite ends by two pairs of Hamamatsu photodiodes MPRS S12572-015P with an active region size of 3x3 mm^2 and a quantum efficiency of about 20%.

The average light output from ~~the~~ two ends of the plate corresponds to about 5 photoelectrons, which makes it possible to reliably detection even particles with a charge Z = 1. Since the intensity of the Cherenkov radiation is proportional to the square of the charge, for fragments with Z = 2, the signal should already be about 20 photoelectrons. Note that the strong dependence of the signal amplitude on the distance to the photodiode can be used to determine the point of passage of the particle through the hodoscope, which makes it possible to determine the coordinates of the particle. Because at the initial stage of the Nuclotron operation beams of light nuclei (carbon) will be used, an additional similar hodoscope with scintillator plates was also constructed.

The FQH will be installed behind the calorimeter and completely cover the calorimeter beam hole. Simulation of Au+Au collisions at 4.5 AGeV with the DCM-QGSM model showed a clear correlation of the FQH signal amplitude and energy deposition in the FHCal. The centrality classes of events can be selected already on trigger level with the use the cut on the hodoscope signal amplitude and the FHCal energy deposition. The FQH and FHCal are ready for first beam runs after finishing the BM@N upgrade.

3.6.5 Upgrade of the forward calorimeter system

It is proposed to extend forward calorimeter system, which include now FHCal and FQH, and add the ScWall (Scintillator Wall) detector to have the possibility to measure not only the centrality and reaction plane in heavy ion collisions but also to measure fragmentation of nucleus. The new experimental fragmentation data for heavy ions collisions are needed to validate fragmentation models used in event generators to simulate the BM@N experiment as well as MPD and CBM experiments. The BM@N is the most suitable experiment for the study of fragmentation in heavy

ion collisions because the BM@N has powerful analyzing dipole magnet deflects the significantly charged components of the spectators and partially separates them from the neutron spectators. The separate measurements of charged and neutron spectators allow us to study the mechanisms of fragmentation and the equation of state of nuclear matter. It is proposed that the measurements of the heavy charged fragments and proton spectators will be performed with the FQH and ScWall correspondingly, while the modified forward hadron calorimeter will be used to measure the neutron spectators. The new forward calorimeter system including the ZDC, FQH and ScWall will be able to measure the fragmentation, centrality and reaction plane in heavy ion reactions. It was shown in the simulation that such detector system will significantly improve the centrality resolution for semicentral events. It is planned that the construction of the ScWall will be performed during 2021-2022 and commissioning of new forward calorimeter system will be done in 2022 and full forward calorimeter system will be used in the BM@N heavy ion physics experiments.

3.6.6 Electro-magnetic calorimeter ECAL

The purpose of the electro-magnetic calorimeter is to study processes with electro-magnetic probes (γ, $e^{\pm}$) in the final state. The physics program of the BM@N experiment with the electro-magnetic calorimeter includes the following studies:

1. Study of known resonanses and search for new resonanses decaying into two γ quanta
2. Study of the yield excess of η^0-mesons in nucleus-nucleus interactions
3. Study of gamma femtometry – two photon interference
4. Study of soft photon spectra at photon energies below 50 MeV, where the yield of γ quanta exceeds in $\sim 4 – 8$ times the theoretical expectations
5. Search for the correlation between the phenomena of pion condensation and abnormal soft photons

The available modules of the MPD ECAL calorimeter will be installed behind the GEM detectors to serve as an electro-magnetic calorimeter in the BM@N experiment.

3.7 Trigger system and beam detectors

3.7.1 Trigger detectors

A system of trigger detectors shown in Fig. 3.7.1 consists of a set of scintillation and Cherenkov beam counters BC1, BC2(T0) and VC multiplicity detectors in the target area BD and SiD; target area multichannel detectors – a scintillation barrel detector BD and a silicon detector SiD; two forward detectors – a detector of charged nuclear fragments of beam ion FD and a forward hadron calorimeter FHCal. The active elements of beam detectors are placed in the vacuum beam pipe upstream of the target. The BC1 is based on BC400B scintillator 100×100×0.25 mm^3 viewed by two PMTs Hamamatsu R2490-07. The VC is based on the same type of PMTs and a scintillator with diameter of 100 mm and 27-mm diam. hole for beam ions.

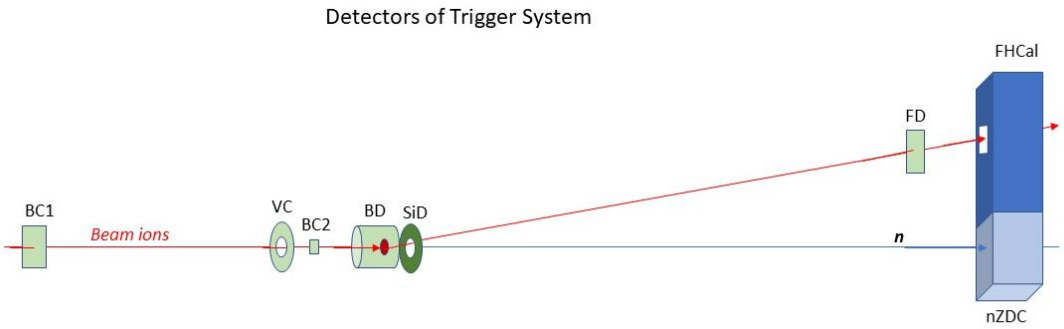

Fig. 3.7.1. A schematic view of the trigger detectors of BM@N setup.

The list of physics triggers with corresponding logic is given below.

Trigger type	Trigger logic
Beam Trigger (BT)	BT = BC1 * VC_{veto} * BC2
No Interaction Trigger (NIT)	**NIT** = **BT** * FD * $nZDC_{veto}$
Min. Bias Trigger (MBT)	**MBT** = **BT** * FD_{veto} * nZDC
Collision Centrality Trigger (CCT)	**CCT** = **MBT** * BD * SiD

The BC2 plays a role of **T0 detector** with a pico-second time resolution and it is used as start detector for TOF measurements. Basic requirements to this detector are: (i) the time resolution better than 50 ps; (ii) ability to work in beams with high intensity up to 10^6 ions/s; (iii) minimal material in the beam line; (iv) high radiation hardness. Two types of radiators are used for registration of beam ions: a thin scintillator BC400B 30 × 30 × 0.15 mm^3 for light nuclei and a thin Cherenkov radiator from optical quartz 40 × 40 × 0.20 mm^3 for heavy nuclei. A scheme of the BC2 is shown in Fig. 3.7.2(left). Scintillation (or Cherenkov) photons are collected to two MCP-PMT XPM85112/A1-Q400 (Photonis), which provide excellent timing and they are able to work in a strong magnetic field. This is important, since the detector should be placed close to the target inside the analyzing magnet of the BM@N.

Active area of the **Barrel detector** has cylindrical shape with dia. 90 mm. It consists of 40 scintillation strips 150 × 7 × 7 mm^3 made of plastic BC418. Each strip is wrapped by aluminum mylar and on one end is connected to a photosensor SiPM Micro FC-60035-SMT, 6 × 6 mm^2 (SensL). Signals from FEE of the BD are sent to the input of the trigger unit T0U. A view of the detector is shown in Fig. 3.7.2(center). The BM@N target is placed inside the BD with position of 40 mm upstream from the end of the BD strips. A lead absorber of δ-electrons produced in the target consists of inner cylinder with thickness of 3 mm and half of disc with thickness of 5 mm and inner and outer radii 40 and 300 mm respectively placed outside of the BM@N acceptance. This geometry of the absorber is the result of background study with MC simulation and this shield provide detector operation with rather small contribution from δ-electrons to the BD response.

The forward angle region is covered by the **silicon detector SiD** which is located downstream from the target at the distance of 120 mm. Signals from the detector front-end electronics are sent to a special module Si-Unit, which determines how many SiD channels had hits in the event.

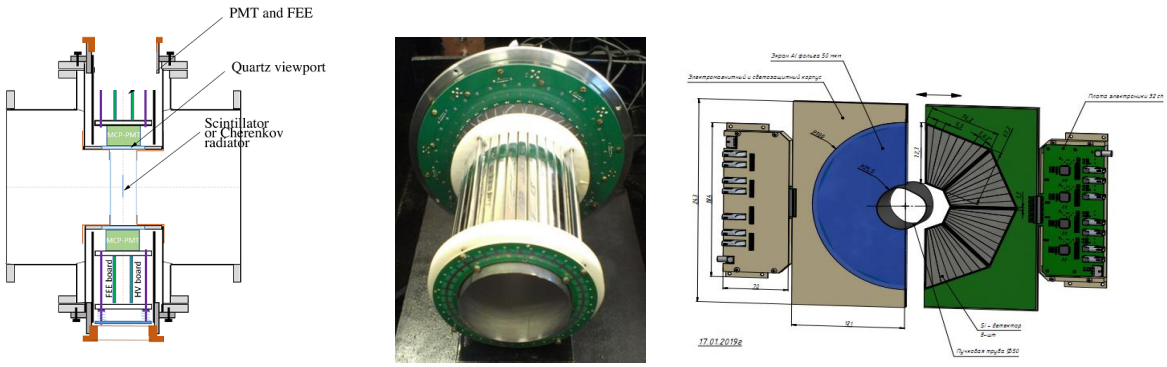

Fig. 3.7.2. The T0 detector design (left), the view of the BD detector (center), the general view of the trigger SiD (right): 8 silicon strip trapezoid detectors and 2 FEE boards.

This information is passed to the trigger unit T0U, where the number of fired channels is compared to a preset trigger threshold. Multiplicity trigger coordinate plane is based on 2 symmetric half-planes, which simplify assembling process around installed beam pipe. General view of these half-planes with read-out boards is shown in Fig. 3.7.2(right). Each of coordinate half-planes consists of 4 detectors 525 μ thickness (total number of strips is 32) with 8 strips located at an angle with an interval of 5.6° and an isosceles trapezoid in shape (45°). The inner diameter of multiplicity

detector is 51 mm and the outer diameter of the circumscribed circle – 186 mm. Trapezoid detectors for the coordinate plane of the multiplicity trigger have been developed and manufactured by RIMST (Zelenograd).

The **forward hadron calorimeter FHCal** is described in detail in the corresponding chapter. Here we consider the FHCal only in view of potentially useful integration of this detector in the trigger system. A special electronics module provides a fast analog pulse for the trigger module T0U. This pulse is the sum of pulse heights of the FHCal modules.

The **nuclear fragment Cherenkov detector FD** has a sensitive area of 160 x 160 mm^2 and it is based on four quartz plates 160 × 40 x 6 mm^3 in dimension each viewed from both ends by a set of four photosensors SiPM MicroFJ-60035-TSV (SensL) with active area of 6 × 6 mm^2. The detector is located behind of the beam hole of the calorimeter FHCal. The detector response is proportional to the sum of fragment charges squared and the pulse is fed to the trigger unit T0U.

The **trigger performance** was studied by MC simulation based on QGSM – GEANT4 code. The obtained results for the main trigger detectors BD, SiD, FD and FHCal are shown in Fig. 3.7.3, 3.7.4 for collisions of 4*A* GeV Au ions with 300- μm Au target. It is clearly seen that the set of target area detectors BD + SiD provides effective triggering on central and semi-peripheral collisions and that the choice of thresholds in the multiplicity detectors helps to suppress the background from δ-electrons produced by beam ions passing through the target. The set of forward detectors FD + FHCal provides additional capability for setting the Min. Bias trigger by selecting interaction events in an even wider range of centrality.

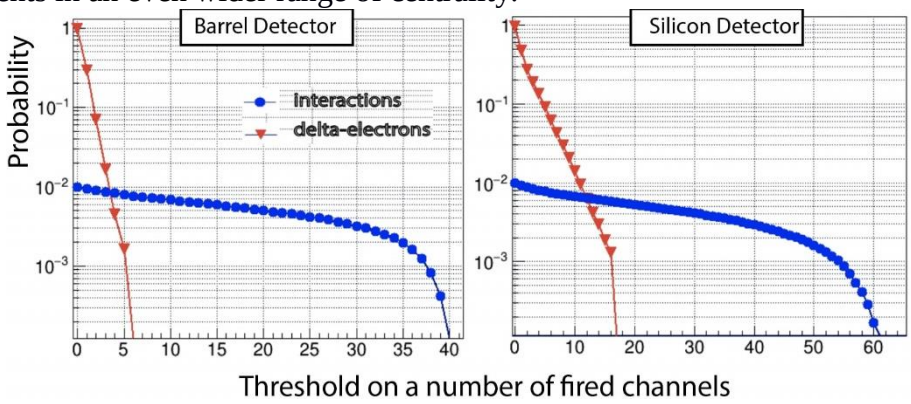

Fig. 3.7.3. The probability of trigger generation by secondary particles of Au + Au interaction (the blue points) and by delta-electrons (the red points) as a function of fired channels for BD and SiD.

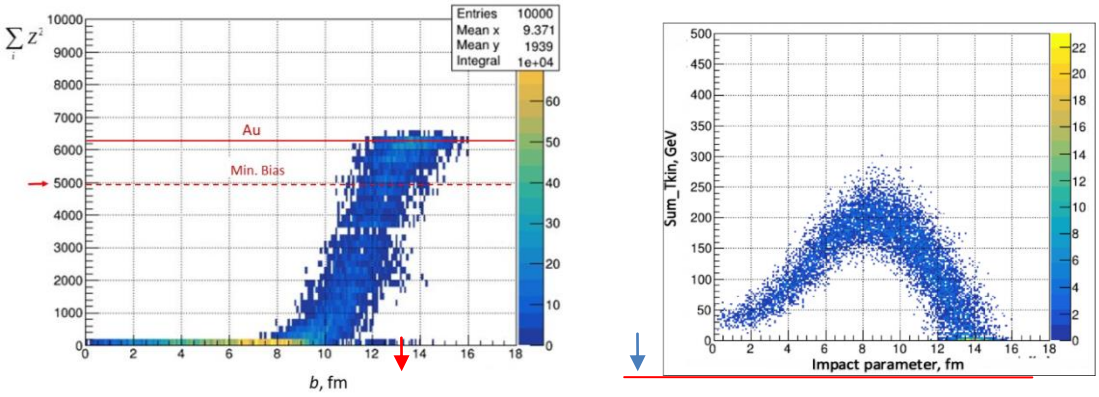

Fig. 3.7.4. The response of the FD to the nuclear fragments (left) and the response of the FHCal (right) as a function of the impact parameter in Au + Au collisions at 4 *A* GeV.

3.7.2 Trigger electronics

The trigger electronics is divided into two parts A and B. The part A is realized as a trigger module T0U based on FPGA. The T0U processes input pulses from the trigger detectors and provides physics triggers in correspondence with programmed logic. The input pulses of the T0U module are analog pulses from BC1, BC2, VC, FD and FHCal plus LVDS pulses from 40 channels of BD and 64 channels of SiD. The module provides fast coincidence of pulses and calculation of

multiplicities of fired channels of BD and SiD. A particular physics trigger is generated, if the response of all detectors participating in its logic satisfies the selection criteria, i.e. all pulse heights and hit multiplicities exceed the thresholds preset for this trigger. The pulses of the physics triggers are fed to inputs of electronics of the part B. The tasks of this part of electronics includes formation of the final BM@N physics trigger from the mixture of triggers with corresponding reduction factors, and generation of special triggers out of spill for calibration of the detectors. In addition, this electronics makes Before/After protection using pulses from the first beam counter BC1. The pulses of trigger detectors are fed to the readout electronics modules TDC, TQDC and Scalers for online monitoring and offline analysis.

3.7.3 Silicon beam tracker

Three beam tracker coordinate planes have been designed to determine the coordinates of incident beam ions. The beam tracker planes are placed inside the beam pipe before the target (Fig. 3.7.5,left). Each plane is based on Double-sided Silicon Strip Detector (DSSD) with the size of 63x63x0.175 mm^3 consisting of 128p+/128n+ strips with a 90˚ stereo angle between strips (Fig. 3.7.5,right). Due to radiation damage in detectors by light and heavy ions, thin float-zone silicon wafers (175 μm) have been chosen for manufacturing DSSD to get low radiation damage and minimize amount of material to reduce multiple-scattering and beam interactions with the detctors.

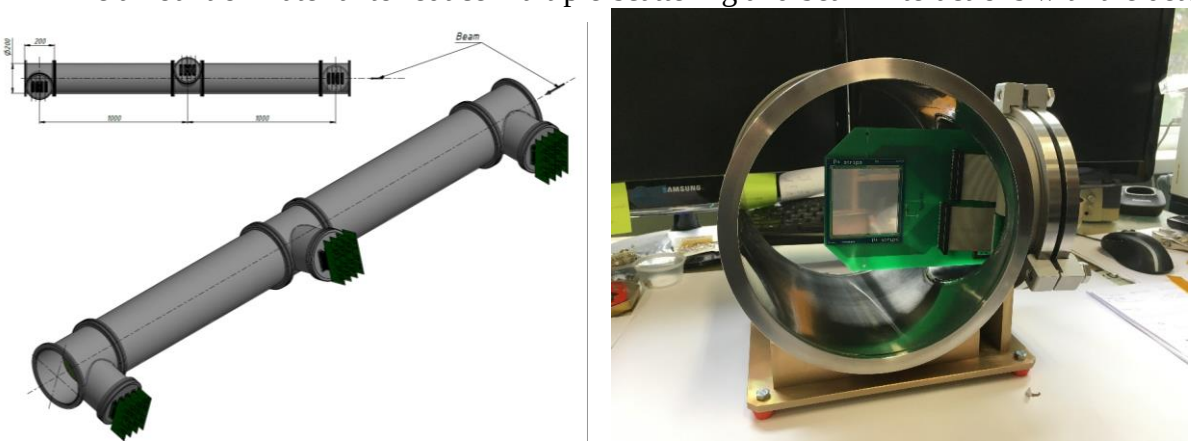

Fig 3.7.5. Left: Beam pipe section with the beam tracker modules. Right: Beam tracker module inside the beam pipe section.

Special requirements for FEE ASIC are ability to register large signal from heavy ions and to sustain high event rate, i.e. wide dynamic range (up to 20 pC), short peaking time (less than 200 ns) for pile-up rejection, at least 64 channels per chip, sample-and-hold from external trigger and multiplexed output (for compatibility with the Si data format transmitted to the BM@N DAQ system). The ASIC VATA64-HDR16 of IDEAS (Norway) was chosen as the closest in parameters and requirements. Based on this ASIC the FEE board of the beam tracker has been developed. The FEE board is installed on the vacuum station flange incorporated in the beam pipe structure and connected via vacuum multi-pin connectors with 256 detector strips.

3.7.4 Silicon beam profilometers

Two beam profilometer planes have been developed for beam tuning during the BM@N runs. The beam profilometer is based on DSSD and placed inside the beam pipe (Fig. 3.7.6). The distance between two planes is approximately 3m. The second plane is placed at 40 cm before the target in front of the beam counter (BC2). The silicon detector has 32p+/32n+ strips with 90˚ stereo angle between strips and 60x60 mm^2 size which is sufficient to fit the beam size on the sensitive area of detector.

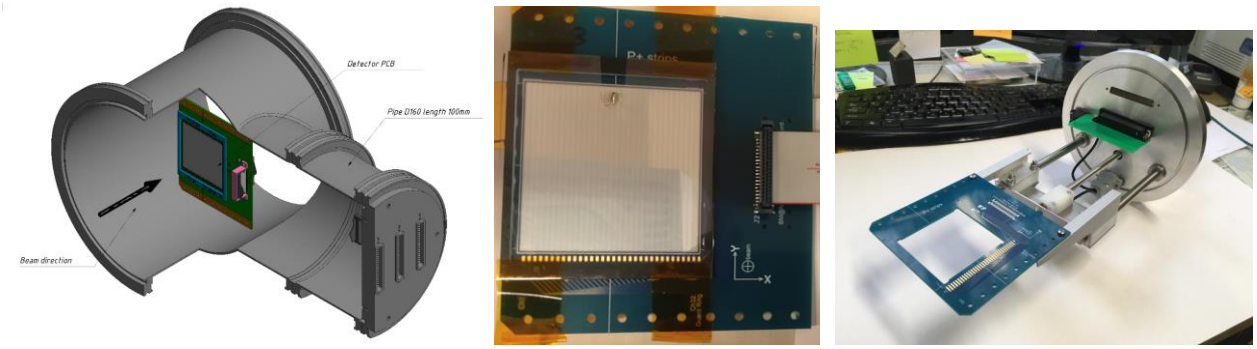

Fig 3.7.6 Detector plane inside the beam pipe (left). Beam profilometer detector plane (center). Beam profilometer mechanical support (right).

The mechanical construction of profilometer planes could be automatic removal from beam zone to a special branch pipe after beam tuning (Fig.3.7.6,right).

Because of the requirement for a wide input charge range two versions of front-end electronics (FEE) for the beam profilometer will be used for light and heavy ions. The front-end electronics is based on VA163 chips (dynamic range is ±750fC) for light ions and VA32HDR11 chip (-35pC ÷ +25pC) for heavy ions. All ASICs are manufactured by IDEAS, Norway. Each chip has 32 inputs of charge sensitive pre-amplifiers (CSA). Each VA163 pre-amplifier output is connected to a shaper (with 500 ns shaping time). The pulse amplitude from all shaper outputs could be multiplexed sequentially to the analogue output buffer by readout diagram.

3.8. BM@N DAQ system and computing

The core function of the DAQ system is realization of data transfer from the detector to the storage system. It includes the data flow from readout electronics to the First Level Processor (FLP) fabric, to the Event Building (EB) and to the Storage System. Main DAQ components are data transfer networks, data processing servers, online storage system, Readout electronics interface, Clock and Time Synchronization (Timing) System and Trigger Distribution.

DAQ system at BM@N consist of 3 large parts:

- Electronic modules, developed by DAQ group, which include DAQ electronics, digitizing modules for all detectors at BM@N, detector control modules, front-end electronics and specific modules;
- Network infrastructure includes White Rabbit Network, Data Transfer Network, Slow Control Network and First Level Processors (FLP).
- Data processing, management, analyzing, utility and control software.

3.8.2. Network infrastructure

Major part of network infrastructure allocated in Modular Data Center (MDC). Experimental area connected to MDC through multiple fiber-optic links. These links are used for hardware control and obtained data transfer to BM@N storage system.

The BM@N Storage System has two stages: the Transient Data Storage (TDS) 285 TB and Permanent Data Storage (PDS) 1.8 PB. It utilizes a two-tier software architecture and data migration from TDS and PDS is transparent to the user. The TDS performs the temporary storage of raw data produced by Event Builder system. The data are recorded to the TDS during data-taking phase of BM@N and is continuously migrated to permanent storage.

White Rabbit network provides sub-nanosecond accuracy and picoseconds precision of synchronization for large distributed systems. The time reference is provided by GPS/GLONASS receiver and backup precision frequency reference (Cesium or Rubidium clock).

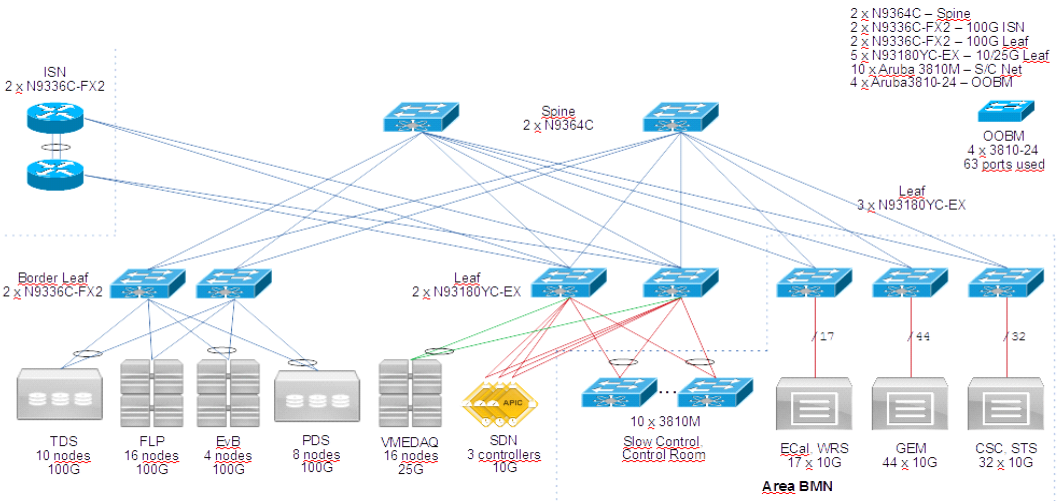

Fig. 3.8.2.2. BM@N DAQ Network

3.8.3. DAQ Software

DAQ software consists of three functional parts: hardware control, event building and run management. All settings of all programs and complete Run setting are stored in Mongo database.

Readout board controls

The set of this programs performs hardware configuration and transition of readout data to event builders.

Event builder

The task of this programs set is to collect data from several client programs (mstream program or another event builder), separate event blocks in every data flow, combines them together per events and further retransmits or writes to the file as united data block.

Run management

These programs performs run preparation, start, stop and correct run flow (event synchronization, correct data acquisition, hardware status monitoring etc.)

Modular structure is common property of all DAQ software. It makes possible to easily add new subsystem or exclude existing from Run. Such excluded subsystems can work autonomous in parallel with main system. The slow control parameters of the detectors are stored via the TANGO interface into a data base. The access to the data base is performed using the software interface developed within the BmnRooT software.

3.9 The BmnRoot framework and analysis software

At present, the activities on the detector and beam line construction are complemented with intensive Monte Carlo simulation studies for optimization of the detector setup. Monte-Carlo simulations aimed in the optimization of the BM@N design have been performed with a sample of generated Au+Au events and lighter ion interactions. For these simulations a dedicated BmnRoot framework intended to process both simulated and obtained experimental data is developed. The same software package is used to define the experimental setup, provides detector performance studies, event simulation, and development of algorithms to be used for digitization, reconstruction and physics analysis of particle collision events with a fixed target. BmnRoot is implemented on the basis of the CERN ROOT 6 environment and object-oriented FairRoot framework of the FAIR collaboration at GSI Institute. BmnRoot is available in the JINR GitLab repository providing GIT Continuous Integration tests to ensure software correctness.

To obtain realistic detector responses very detailed geometrical description of each of the subdetectors has been performed. To define the detector geometries, the ROOT format in the form of a tree containing basic geometric volumes is mainly used in BmnRoot. A complementary XML file including detailed parameters of the detector structure, which are required for realistic simulation, digitization, hit reconstruction, is used. To study physics feasibilities of the experiment, BmnRoot supports a wide list of Monte-Carlo event generators with the proper physics effects, such as DCM-QGSM and DCM-SMM to provide realistic particle and energy distributions, investigate physics effects and to simulate different versions of the setup. Particle propagation through the detectors in simulation is performed using Geant 3 or Geant 4. The Fluka transport package is used to estimate radiation doses and neutron fluxes in the BM@N experimental zone.

Event data processing in the BmnRoot framework are realized via ROOT macros, which perfrom simulation, digitization, reconstruction and various physics analyses. In turn, their inner tasks, such as detector response functions, tracking, particle identification and others, are implemented as a chain of FairRun Manager Tasks. The steps of event data processing in the BmnRoot framework are shown in Figure 3.9.1.

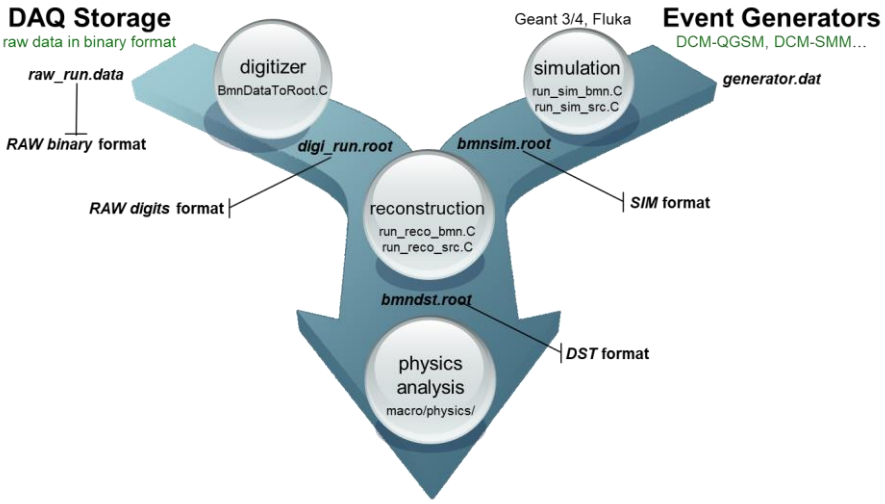

Fig. 3.9.1. Event data processing in the BmnRoot framework

Raw experimental data obtained from DAQ in a binary format are digitized and converted into the ROOT format by a digitizer (ROOT digitizing macro). The obtained digit file contains a digit run header and hierarchical ROOT tree with event headers and digits grouped by events for all the detectors. Reconstruction macros use developed reconstruction algorithms and restores the information on produced particles registered by the detectors, their momenta, types, tracks, and other kinematic parameters. The restored information is saved in a DST (data summary tape) file containing detailed output of the reconstruction, such as ROOT branches with hits, particle tracks, primary vertex and others. For the BM@N data, it is planned to use two formats of reconstructed data: the current DST and future miniDST containing only sufficient information for physics analyses. In the last step, various physics analyses of the reconstructed event data are used to investigate the physical properties of the nuclear matter produced at the collisions.

The BM@N Condition Database was developed on PostgreSQL as comprehensive data storage for offline data processing. It stores information on the BM@N runs, recorded experimental data, as well as detectors, arbitrary parameters of different types (configuration, calibration, parameter, algorithm) and simulation files obtained by event generators. The BmnRoot environment uses the developed database interface to get information for detector simulation, raw data processing, event reconstruction and physics analysis tasks. The Web interface of the Condition Database provides convenient viewing and changing the data of the experiment over the Web, and visualizing summary statistical information on the BM@N conducted runs.

Mass production of simulation, raw data digitization, event reconstruction and physics analysis tasks are performed offline at distributed systems of the experiment. For distributed data processing

of the BM@N events, three computing platforms are currently employed. The Central Information and Computer Complex (CICC) in the Laboratory of Information Technologies provides two queues (Torque scheduler) in small parts of the Tier-1 and Tier-2 centres (on average is about 300 cores for BM@N). The EOS mass storage of the CICC complex is allocated with 1 PB space for the experiment. The Govorun supercomputer is a new part of the HybriLIT heterogeneous platform, which is a computing element of the CICC JINR aimed at acceleration of theoretical and experimental research at JINR. BM@N data processing tasks are also solved via the SLURM scheduler on the Intel Xeon queue of the Govorun containing about 400 logical cores. The NICA in the Laboratory of High Energy Physics provides 1 PB of the EOS distributed file system to organize the data storage for the BM@N experiment, and GlusterFS weekly storage. The Sun Grid Engine scheduling system of the cluster distributes user jobs limiting the number of running tasks to 400 per user, as well as for BM@N mass production.

All required packages, such as, FairSoft, FairRoot, BmnRoot, have been deployed and configured on a central software CVMFS repository of the CICC complex, which is accessible on all the cluster platforms (except the NICA cluster) for distributed processing of the BM@N data. The distributed computing platforms have been used to perform full reconstruction chain, which requires reconstructed data for all source raw data files, for the conducted BM@N Runs. But the feature of the current computing platforms is that they provide different batch systems and separated data storages. To combine all the resources into one computing system, workflow services for distributed BM@N data processing are being implemented.

The preliminary results obtained for the current configuration of the BM@N experiment show that for one month of the BM@N operation a storage size of approximately 340 TB is required for raw data and 85 TB to save reconstructed digits and DST files (3 software versions). Assuming 4 months of BM@N operation per year, the distributed storage should allow allocating up to 1.7 PB per year for BM@N data. It is important to note that the size of BM@N event is directly proportional to multiplicity, which is a function of interaction centrality. Furthermore, the amount of data taken in experimental runs varies with the detector setup, collision system and trigger conditions.

3.10 BM@N experimental zone

A reference metrological grid of the BM@N experimental zone was created by specialists of Industrial Measurements by a set of 3D measurements. The following works have been performed: the full BM@N coordinate system is fixed; measurements of the coordinates of reference marks and basic elements have been made; measurements of the relative positions of the BM@N elements have been done. For realization of the physical program with heavy ion beams with intensities few 10^6 ion/s additional reinforced concrete blocks for the personnel biological protection should be installed. Simulations of radiation protection of the experimental zone were performed using FLUKA program to optimize the concrete shielding.

3.10.1 Vacuum beam pipe within BM@N

A vacuum beam pipe will be integrated into the experimental setup to minimize the amount of scattering material on the way of heavy ion beam. The beam pipe will consist of three parts: section before the target, inside the analyzing magnet and after the analyzing magnet. The beam pipe before the target is produced from stainless steel and consists of standard vacuum modules and boxes for the beam detectors (Fig.3.10.1).

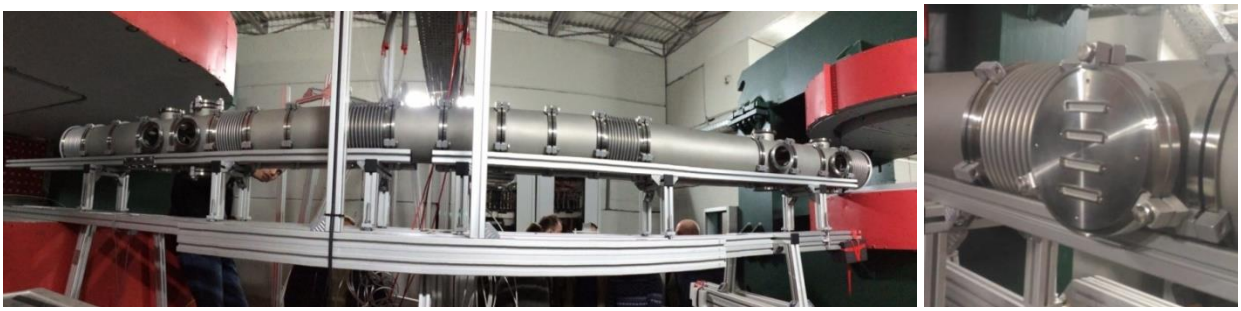

Figure. 3.10.1. Beam pipe before the target and boxes for the beam detectors.

This configuration of the beam pipe was designed and manufactured and tested by LLC “Vacuum systems and technologies” (Belgorod, Russia).

Figure. 3.10.2. Target station. Photo (left,center) and 3D model (right).

After the 1st beam pipe section the target station will be located. It allows us to expose 4 film targets and interchange the targets without breaking the vacuum using the pneumatic cylinders produced by FESTO. The model and photo of the target station are presented at Fig.3.10.2.

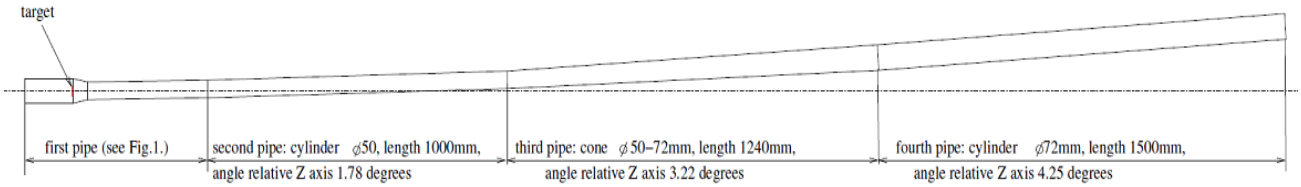

Figure.3.10.3 Technical design of the carbon beam pipe to be placed inside the analyzing magnet.

A carbon beam pipe will be installed inside the analyzing magnet. It will consist of four parts shown in Fig.3.10.3. Such configuration allows us to install different set-ups of tracking detectors using demountable flangeless connectors (Fig.3.10.4). The total length of the carbon beam pipe is 5 m. The thickness of the walls is 1 mm. It is design to sustain vacuum up to 10^{-3} Torr.

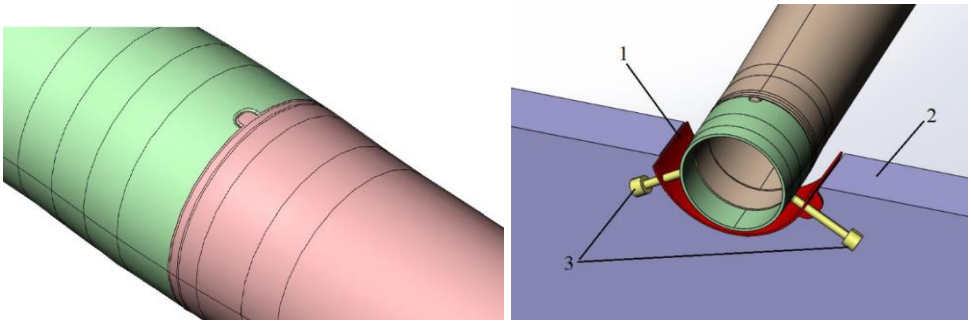

Figure.3.10.4. 3D models of the dismountable flangeless connection (left) and the support scheme of the carbon beam pipe in the GEM beam hole (right).

The beam pipe after the analyzing magnet will be made of aluminum with a diameter of 125 mm and a wall thickness of 1 mm.

3.10.2 Spectrometrical Magnet

The measured map of the magnetic field of the SP-41 analysing magnet is illustraded in Fig.3.10.5.

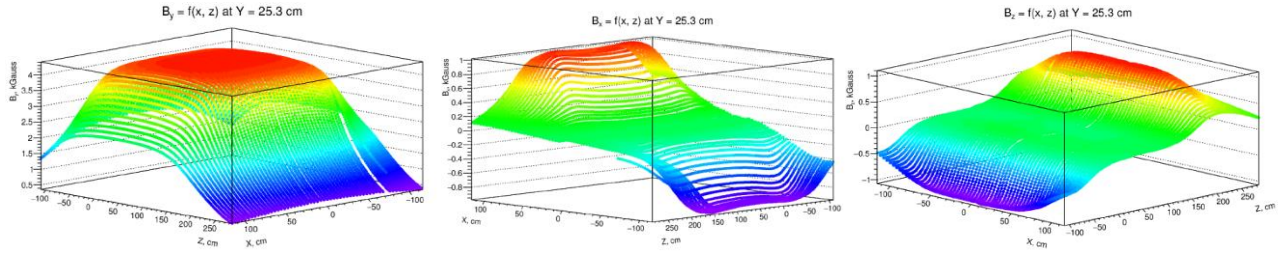

Figure 3.10.5. Two dimentional (X-Z) distributions of the magnetic field components By, Bx, Bz (kGauss) measured in the horizontal plane at Y=25 cm from the magnet median plane.

3.10.3 Beam line to BM@N

Horizontal and vertical beam size envelopes (2σ) on the way to the BM@N area are shown in Fig.3.10.6. The horizontal and vertical profiles of the krypton beam at 1 m in front of the target are also given. The X / Y sizes (sigma) of the carbon, argon and krypton beams measured at 1 m in front of the target in the BM@N technical runs are summarized in the table below.

	C^{12} 2017	Ar 2018	Kr 2018
σ_X =	6 mm	5 mm	5.3 mm
σ_Y =	4.9 mm	5 mm	3.2 mm

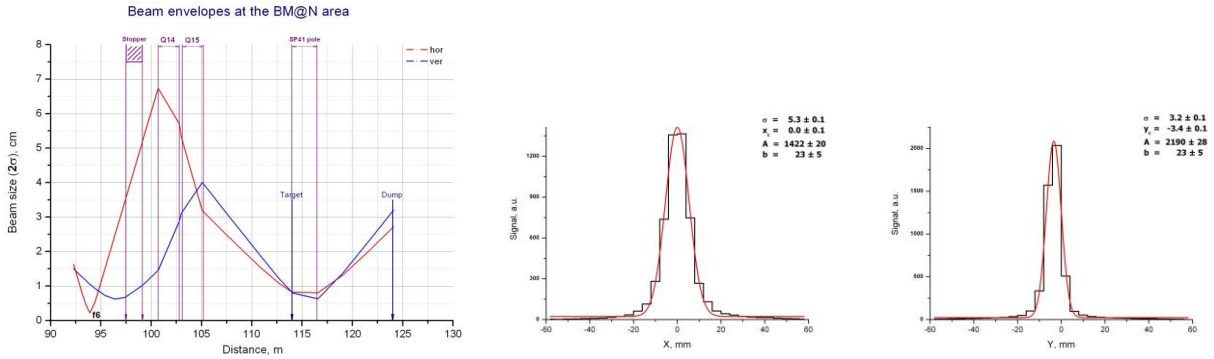

Figure 3.10.6. Left plot: Horizontal and vertical beam size envelopes (2σ) in the BM@N area. The positions of the target, the edges of the pole of the spectrometrical magnet and the beam dump are shown. Central and right plots: Horizontal and vertical profiles of the krypton beam at 1 m in front of the target.

[3.10.1] http://bmnshift.jinr.ru/wiki/lib/exe/fetch.php?media=rukoyatkin_4bmncounsil_01.ppt

4. Estimated uncertainties and risks in the Project

We consider the following uncertainties and risks in the project realization:

- Due to a possible delay with the construction of the full vacuum transport channel from the Nuclotron to BM@N the start of heavy ion beam runs could be postponed. Interactions of

the heavy ion beam in the air and beam channel elements could cause unacceptable halo background and a wider spread of the beam for the efficient detector operation. The installation of a collimator would reduce the level of background originated from the transport channel.

- Uncertainty in putting into stable routine operation of the Booster-Nuclotron accelerator complex could cause delay of the start of the heavy ion program.
- Putting the NICA collider into operation could limit the capacity of the accelerator division to perform experimental runs at the Booster-Nuclotron complex. As a result the accelerator time requested to fulfill the project goals could be achieved later in time.
- Probable delay and long commissioning phase of the installation and putting into operation of the large aperture silicon tracking system STS. As a result, the high intensity heavy ion beam runs with the final BM@N configuration could be delayed.
- A fast FEE electronics for GEM and CSC readout in the high intensity heavy ion beam runs could be not available due to the delivery restrictions. As a result, BM@N will be operated at the beam intensity of few 10^5 Hz.
- Probable delay in the construction of two big CSC chambers of the outer tracking system. The existing DCH drift chambers could be used instead for the middle weight ion beams.
- The response of the beam silicon and trigger detectors could deteriorate due to high ion fluxes. Spare exemplars of the detectors are foreseen for replacement.

5. Estimated expenditures for the Project

Expenditure items	Total cost / resources	1 year 2022	2 year 2023	3 year 2024	4 year 2025	5 year 2026
Direct project expences						
1. Accelerator, hours	14000	2000	3000	3000	3000	3000
2. Computing (proc*hours) / mln	100	15	15	20	25	25
3. Laboratory workshop, hours	2600	600	600	600	400	400
4. Laboratory design buro, hours	1500	500	300	300	200	200
5. Equipment, materials, kUSD	2670	1250	430	350	330	310
6.Research carried out under contracts, kUSD	250	50	50	50	50	50
7.Traveling allowance, kUSD, including:	750	150	150	150	150	150
a) non-ruble zone countries	250	50	50	50	50	50
b) ruble zone countries	250	50	50	50	50	50
c) protocol-based	250	50	50	50	50	50
Total direct expenses, kUSD	3670	1450	630	550	530	510